Laser powder bed fusion of SS316L-IN718 functionally graded materials: Processing, microstructure, and properties

Materials Science & Engineering A 934 (2025) 148341

Contents lists available at ScienceDirect

Materials Science & Engineering A

journal homepage: www.elsevier.com/locate/msea

Laser powder bed fusion of SS316L-IN718 functionally graded materials: Processing, microstructure, and properties

Reza Ghanavati [a,b], Abdollah Saboori [a,b,*], Elżbieta Gadalińska [c], Sara Bagherifard [d], Luca Iuliano [a,b]

[a] Department of Management and Production Engineering (DIGEP), Politecnico di Torino, Corso Duca Degli Abruzzi 24, 10129, Torino, Italy
[b] Integrated Additive Manufacturing Center (IAM@PoliTo), Politecnico di Torino, Corso Castelfidardo 51, 10129, Torino, Italy
[c] Academy of Sciences of the Czech Republic, HiLASE Centre, Institute of Physics, Dolni Brezany, Czech Republic
[d] Department of Mechanical Engineering, Politecnico di Milano, Via La Masa 1, 20156, Milano, Italy

ARTICLE INFO

Keywords:
Additive manufacturing
L-PBF
FGMs design
Crystallographic texture
Residual stress
Mechanical behavior

ABSTRACT

Functionally Graded Materials (FGMs) development has recently accelerated thanks to Additive Manufacturing (AM) technology, as its layer-wise manner flexibly enables the production of complex high-performance FGMs. More recently, the Powder Bed Fusion (PBF) process has been preferred over other AM techniques owing to its unique advantages in discovering a new generation of FGMs. Therefore, herein, an innovative approach for the composition control has been introduced to fabricate SS316L-IN718 FGMs using a standard laser powder bed fusion (L-PBF) process and then investigated to realize the effects of the design and processing conditions on the FGM's microstructure and mechanical properties. The results demonstrated that the high density of the samples contributed to the reliability and reproducibility of the process. Nevertheless, the FGM with 25 wt% gradient steps (F25) suffered from severe solidification cracking in the 75-25 composition region, formed around oxide inclusions at continuous micro-segregations along grain boundaries leading to the low-temperature eutectic reaction of $L \rightarrow \gamma +$ Laves. Furthermore, the dynamics of the residual stress variations along the building direction were effectively modified by the FGM design from a sharp change in the direct transition structure (F0) to a smooth change in the F25 structure. However, the sample with a 50 wt% mixed intermediate region fabricated by optimum processing parameters (F50IN.Opt) showed the best mechanical properties (610 MPa tensile strength, 31.5 % elongation) against the F25.Opt structure (580 MPa tensile strength, 11 % elongation) with a dominant brittle fracture mechanism due to rapid propagation of the pre-existed solidification cracks in its susceptible region.

1. Introduction

The ever-growing demand for higher performance is the main driving force in exploring and developing new materials. Functionally graded materials (FGMs) are a class of advanced engineering materials that offer specific local properties through gradual changes of structural constituents (*e.g.*, chemical composition, microstructure, and density) in a selected direction(s) [1,2]. This unique tailored characteristic inspired by our natural surroundings has made them a prominent candidate in the materials selection for critical service conditions since a gradual transition instead of a sharp interface throughout a part can cause higher performance and longevity of the engineering structure. Depending on the FGM size, several manufacturing methods have been conventionally utilized, including powder metallurgy and centrifugal casting for bulk FGMs as well as physical/chemical vapor deposition and thermal spray to produce thin FGMs [1–4]. Nevertheless, some drawbacks, such as difficult control of density, simple part geometry, serious environmental harms, and economic issues, have caused FGMs to be held back from their potential. In the last decade, the emergence of additive manufacturing (AM) technology in the production of FGMs has led to a new horizon of development in various application fields since AM can provide unprecedented advantages over conventional manufacturing (CM) methods, which include limitless design freedom, high level of customization, more sustainability, and shorter supply chain [2,5–7].

* Corresponding author. Department of Management and Production Engineering (DIGEP), Politecnico di Torino, Corso Duca Degli Abruzzi 24, 10129, Torino, Italy.
E-mail address: Abdollah.saboori@polito.it (A. Saboori).

https://doi.org/10.1016/j.msea.2025.148341
Received 14 January 2025; Received in revised form 11 April 2025; Accepted 11 April 2025
Available online 15 April 2025

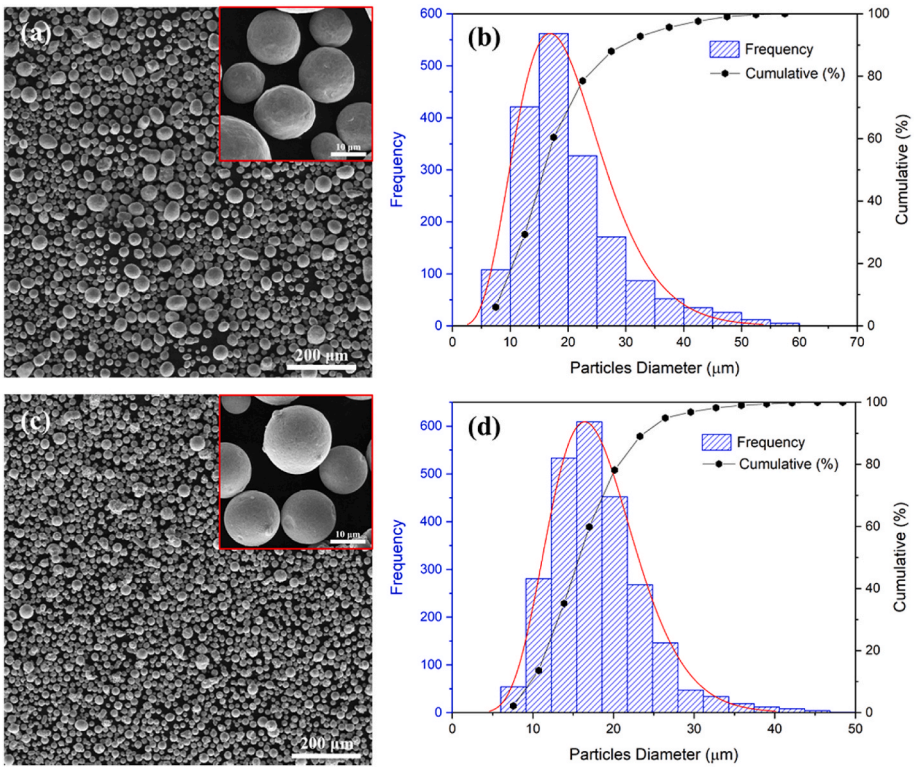

Fig. 1. Morphology and size distribution of powder particles: a, b) SS316L and c, d) IN718.

Table 1
Chemical composition analysis of used SS316L and IN718 powders (wt. %).

Element	Fe	Ni	Cr	Mn	Si	Mo	Nb	Ti	Al
SS316L	Bal.	10.6	17.2	1.7	0.6	2	–	–	–
IN718	17.3	Bal.	19.7	–	–	3.4	5.1	1	0.8

Although among metal AM processes, directed energy deposition (DED) is more popular to produce compositional FGMs [8], it has been lately demonstrated that powder bed fusion (PBF) is also capable of fabricating this kind of FGMs with its inherent features such as higher resolution, finer composition control, and much less post-processing required unlike DED [9]. Hence, several attempts have been made to adapt PBF for the fabrication of FGMs from various base alloys such as stainless steel 316L-tool steel H13 [10], Ti6Al4V-Inconel 718 [11], W-Cu alloy [12], $TiAl_x$ [13], Ni-Ti [14], Invar 36-stainless steel 316L [15], and CuCrZr-stainless steel 316L [16]; these studies have provided different in-house developed mechanisms for PBF machines to realize such FGM structures, though there is still a serious lack of a reliable generalized solution in this context.

Multi-functionality at a reasonable cost, as well as good printability, have made stainless steel (SS)-Inconel (IN) multi-material, particularly SS316L-IN718 FGM, among the most interesting practical FGM structures acquired by AM techniques which can be used in crucial energy industries [17,18]. Insofar as a wide spectrum of studies has been carried out on FGMs by L-DED process ("L" denotes laser as the heat source) from different aspects, including structural integrity and mechanical properties [19], design challenges considering the risk of cracking [20,21], multi-physics modeling of the process [22], the effect of post-heat treatment on microstructure-property correlation [23,24], hot corrosion resistance [25], and high-temperature fracture behavior and creep resistance [26]. In contrast, only a few studies have addressed SS-IN multi-material manufactured by PBF, interestingly, mostly in the simplest design, *i.e.,* bimetal, rather than FGM. In this regard, Hinojos et al. [27] demonstrated the feasibility of joining IN718 to SS316L, and vice versa, by electron beam (EB)-PBF. They found improved joint qualities compared to traditional dissimilar welding despite some defects arising at both interfaces. Mei et al. [28] reported good metallurgical bonding and a superior combination of mechanical properties for the SS316L-IN718-SS316L structure produced by laser (L)-PBF, though multiple cracks and pores were observed on the SS316L side close to the interfaces, proposing the need to optimize process parameters not only for each material but also at the interface. This issue and its solution have been ascertained in other similar works utilizing *in-situ* monitoring by high-speed X-ray imaging [29] and extensive interfacial microscopy analysis [30]. In a distinct work, Duval-Chaneac et al. [31] studied the fatigue behavior of SS316L-IN718 layered structure fabricated by L-PBF using a three-point bending test and revealed the crack growth mechanisms of trans-granular, combination of trans- and inter-granular, and inter-dendritic decohesion within IN718, SS316L, and the dissimilar interface layers, respectively. Moving forward from simple to special designs, Wits and Amsterdam [32] demonstrated a gradual material transition through in-process alternating material layers utilizing an adapted recoater following a post-heat treatment to enhance elemental diffusion. Errico et al. [33] devised an ad-hoc partitioning blade inside the powder feedstock chamber to fabricate a horizontal intralayer multi-material and an *in-situ* and real-time optical monitoring system to avoid the deviation of materials interface from the ideal linear profile. Further, other researchers developed a custom powder dispensing system enabling the mixing powders in desired proportions and creating a composition gradient perpendicular to the building direction, which indicated suitable portions of SS316L-IN718 graded alloy for structural applications where the IN718 content exceeds 25 wt% [34].

Despite limited but noteworthy previous efforts and findings in this context, there is still the lack of an easily applicable and reliable L-PBF process in FGMs production beyond the self-developed systems with additional tooling, and the reported issues on their controllability, repeatability, and productivity as well as their limitation to be applied to more complex configurations rather than the simple bimetal design. Therefore, we have recently demonstrated the capability of a

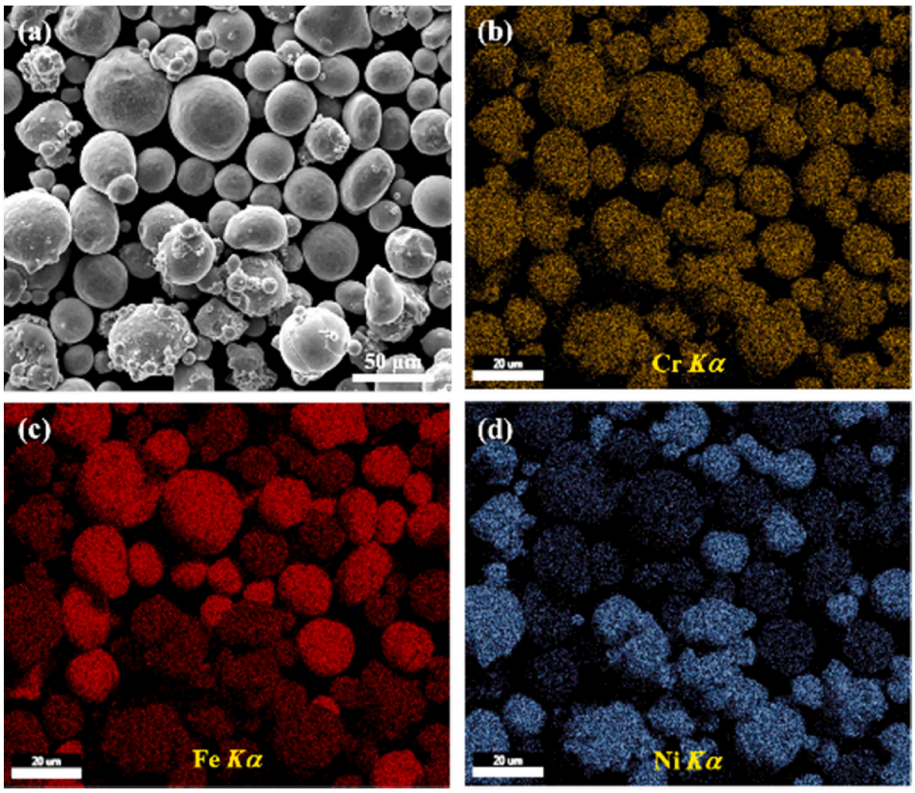

Fig. 2. a) Micrograph and b-c) distribution maps of the main elements (Cr, Fe, and Ni, respectively) of the powder mixture with a 50/50 wt ratio of SS316L and IN718 feedstocks.

Table 2
Experimental design of the L-PBF process parameters for thin-wall SS316L-IN718 bimetals.[a].

Set no.	P (W)	V_{SS316L} (mm/s)	V_{IN718} (mm/s)	t_{SS316L} (mm)	t_{IN718} (mm)	LED_{SS316L}[b] (J/mm)	LED_{IN718}[b] (J/mm)	Scanning strategy
1	95	600	900	0.025	0.02	0.16 (L)	0.10 (L)	Uni/bidirectional
2	95	500	800	0.025	0.02	0.19 (M)	0.12 (M)	Uni/bidirectional
3	95	400	600	0.025	0.02	0.24 (H)	0.16 (H)	Uni/bidirectional

[a] The printing order was first SS316L and then IN718, with 80 layers for each alloy.
[b] L: Low, M: Medium, H: High.

commercially available L-PBF machine in the design and development of SS316L-IN718 FGMs through an innovative concept without adding any special modules [35]. In the following, the present study aims to elucidate the interrelated aspects of processing, microstructure, and properties in L-PBF of SS316L-IN718 FGMs and establish the most desirable FGM design with respect to printability (herein, *i.e.,* cracking susceptibility) and performance.

2. Materials and methods

2.1. FGM design and processing

Gas atomized powders of SS316L and IN718 were used as the materials feedstock with spherical morphology and Gaussian particle size distribution (left skewness, average size of 20 μm) individually shown in Fig. 1 with their chemical composition from the supplier's data presented in Table 1. Three powder mixtures with weight ratios of 50/50, 75/25, and vice versa were prepared from the primary alloys through mechanical mixing in containers for 12 h at room temperature. Fig. 2 shows the micrograph and elemental distribution maps of a sampled powder mixture from the 50 % SS316L and 50 % IN718 wt ratio. An AISI 316L stainless steel plate with the dimensions of 100 × 100 × 10 mm^3 was used as the building platform.

A commercial L-PBF machine of Concept Laser Mlab Cusing-R (General Electric, USA) equipped with a 100 W continuous wave fiber laser was employed to fabricate the FGM samples. For this purpose, the powder reservoir of the machine was carefully loaded with inverse gradient composition for every FGM design along the building direction (BD) so that the first powder composition to be spread by the recoater would be the bottommost composition region in the FGM, and likewise the last powder composition for the topmost composition region in the FGM. More details on the manufacturing process can be found in our previous work [35]. In order to identify the process parameters window, the design of experiment (DoE) was carried out for thin-wall (TW) SS316L-IN718 bimetals according to Table 2 with three levels of linear energy density (*LED*) per alloys in uni/bidirectional scanning strategy:

$$LED_{ij} = \frac{P}{V_{ij}} \tag{1}$$

where P is the laser power, V is the scanning velocity, and i and j indicate set numbers and the base alloys, respectively. As can be seen in Fig. 3a, some TW samples fabricated by the high *LED* parameters (set no. 3) were delaminated during the process. Hence, the low and medium *LED* parameters (sets no. 1 & 2) were selected to produce 10 × 10 × 5 mm^3 cubic bimetals. Fig. 3b demonstrates that the cubic bimetals were successfully and reproducibly made without any noticeable external

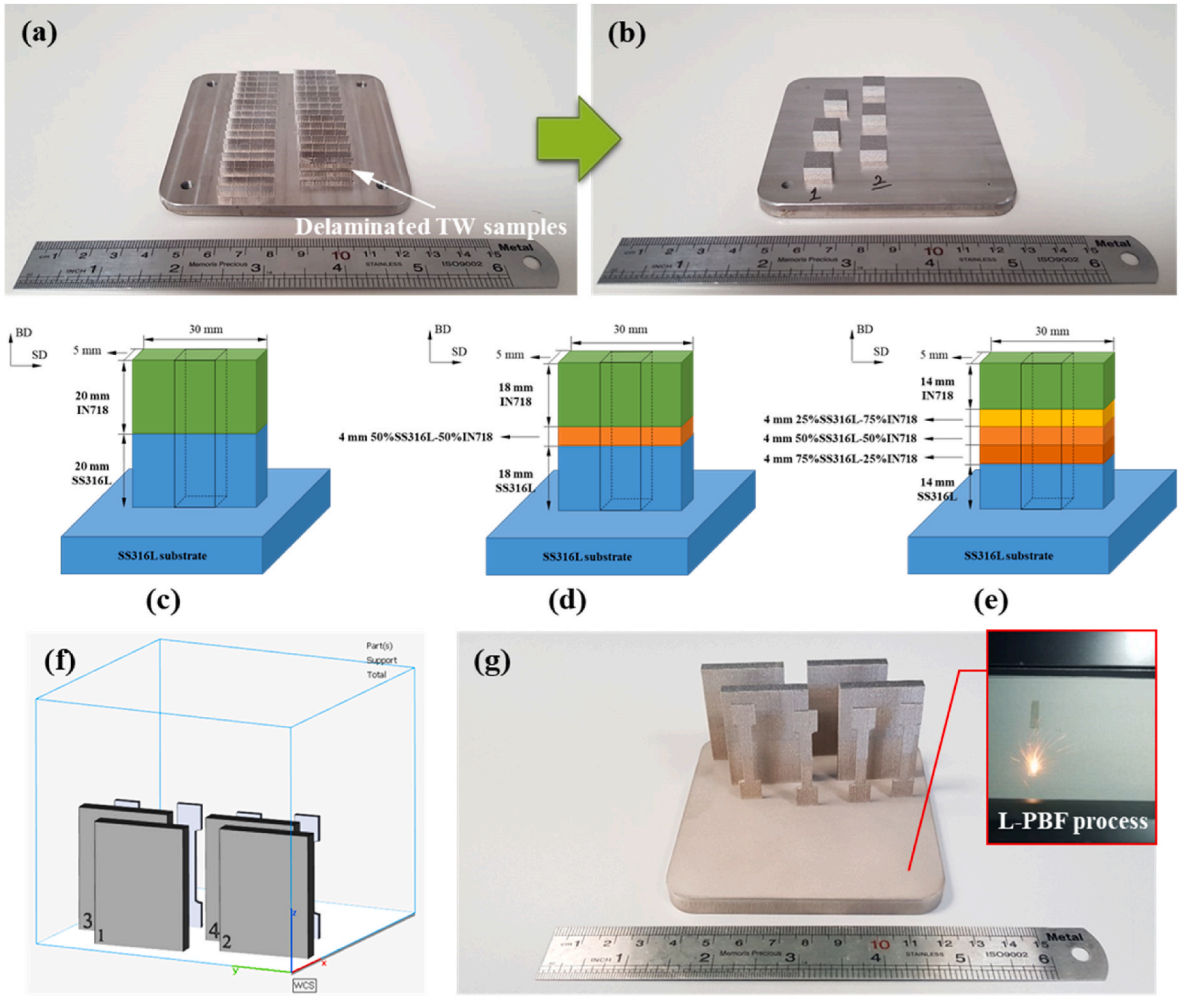

Fig. 3. a) Experimental design for thin-wall (TW) bimetals, b) successful production of bimetal cubes using the selected sets of process parameters, c, d, e) FGM designs: F0, F50, and F25, respectively, f) parts design [35], and g) L-PBF fabricated F0.Opt samples.

Table 3
Process parameters for the bulk SS316L-IN718 FGMs.

Set no.	*P* (W)	*V* (mm/s)	*d* (mm)	*t* (mm)	*VED*[a] (J/mm^3)	Scanning strategy	Composition region
1	95	500	0.084	0.025	90 (Opt)	Stripe 0/90°	SS316L, 75-25
	95	800	0.05	0.02	119 (Opt)	Stripe 0/90°	50-50, 25/75, IN718
2	95	600	0.084	0.025	75.4 (L)	Stripe 0/90°	SS316L, 75-25
	95	900	0.05	0.02	106 (L)	Stripe 0/90°	50-50, 25–75, IN718

[a] Opt: Optimum, L: Low.

defects. As a result, the viability of these parameter sets was confirmed and considered for the fabrication of the intended FGM designs.

Three FGM designs, including direct transition (F0), 50 wt% mixed intermediate region (F50), and 25 wt% incremental replacement with equal thicknesses (F25) between the terminal alloys were implemented as depicted in Fig. 3c, d, and e, respectively. For every FGM, four 40 × 30 × 5 mm^3 blocks and four 40 × 8 × 1.36 mm^3 rectangular tensile samples (gauge section: 20 × 4 mm^2) were sketched (Fig. 3f) and fabricated by two sets of process parameters (based on the previous DoE) as provided in Table 3, resulting low (L) and optimum (Opt) volumetric energy densities (*VED*) for each composition region:

$$VED_{ik} = \frac{P}{V_{ik} \cdot d_{ik} \cdot t_{ik}} \tag{2}$$

where *d*, *t*, *i*, and *k* denote the hatch distance, layer thickness, set number, and composition region, respectively. Thus, the abbreviation of L/Opt was added to the FGM designations (F0, F50, and F25) to indicate the *VED* level used for fabrication. For instance, Fig. 3g illustrates F0 samples fabricated with the optimum *VED* for each composition region (F0.Opt). Also, it should be noted that the 50-50 intermediate region in the F50 design was made once with the process parameters of the SS316L region (named as F50SS) and another time with the process parameters of the IN718 region (named as F50IN), the evaluations of which showed fewer internal defects in the F50IN. Therefore, that region in the F25 design was fabricated using the same process parameters as the IN718 region.

2.2. Characterization and measurement

To study the fabricated FGM samples, they were first cut off from the building platform using wire electrical discharge machining (WEDM), and the block-type samples were chopped longitudinally into three

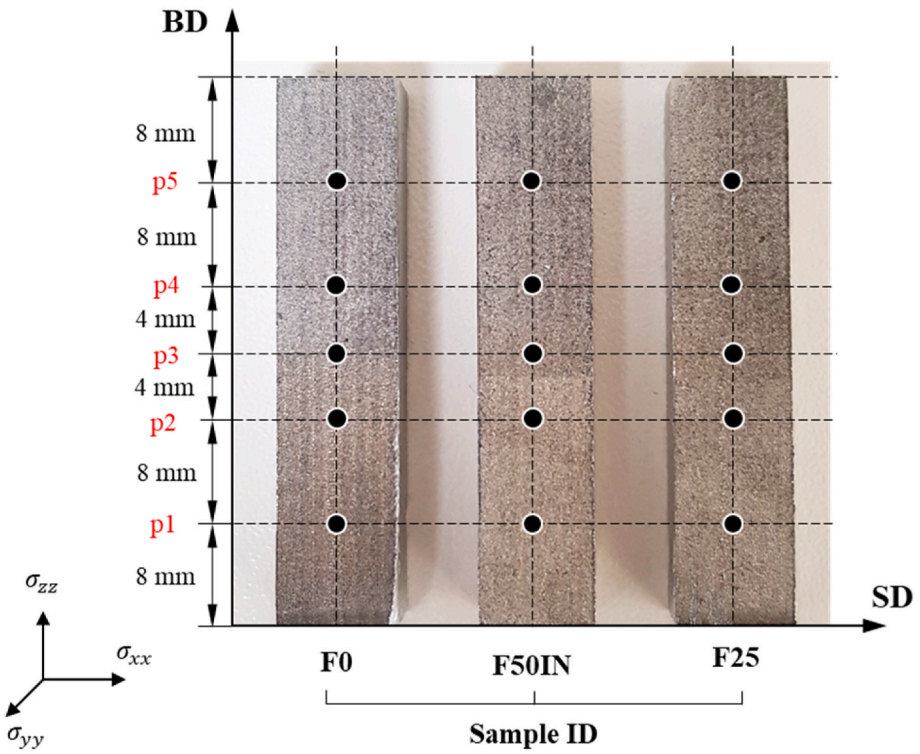

Fig. 4. Points localization on the FGM samples for subsequent residual stress measurements by XRD.

Table 4
XRD parameters for surface residual stress measurements on the points shown in Fig. 4.

Parameter	Value
Measurement spot size (mm)	1 × 1
Expected approx. 2 θ (°)	146.65
Tilt axis	omega
Range of tilting	positive + negative
PHD lower level (%)	31
PHD upper level (%)	100
$Sin^2\ \psi$ step	0.15
No. of ϕ directions	1
2 θ range (°)	10.8194
2 θ step size (°)	0.1050422
Measurement time for one step (s)	13,500
Scanning speed (°/s)	0.001984
Number of steps	103

sections as marked with the dashed lines on Fig. 3c–e for various characterizations and measurements. X-ray computed tomography (CT, GE Phoenix v|tome|x s) was conducted on the tensile samples with a voxel size of 12 μm, and the results were analyzed by VGStudio Max 3.4 software. Standard metallographic procedures were applied to the cross-section of each FGM after being etched by dipping for 10 s in an aqua-regia (1:3 HNO_3:HCl) solution to reveal microstructural features through optical microscopy (OM, Leica DM6 M, Germany) and scanning electron microscopy (SEM, FEI Quanta 200, USA). Moreover, the constituent elements distribution, segregation, and possible phase compositions were analyzed by an energy-dispersive X-ray spectroscope (EDS, Oxford Ultimax 65, UK) detector, while the crystallographic texture, orientation, and crystal defects were investigated using an electron backscattered diffraction (EBSD, Oxford C-NANO, UK) detector, both operating within the chamber of a field-emission scanning electron microscope (FE-SEM, Zeiss Sigma 500, Germany). For the EBSD analysis, the surface of the specimens underwent additional preparations, including auto-polishing with 3 and 1-μm diamond suspension and electrochemical polishing in 6 vol% $HClO_4$ + 94 vol% CH_3COOH solution at 50 V for 10 s. EBSD scans were performed over areas of 1.8 × 0.6 mm^2 along the building direction from the interface of the FGM regions (plus an area of 55 × 15 μm^2 from a cracked zone) with 3 μm step size, and the collected data were processed and interpreted by HKL-Channel 5 software. Furthermore, residual stress variations caused by the L-PBF process and compositional gradients were measured utilizing the X-ray diffraction (XRD) technique and the standardized $sin^2\ \psi$ method [36,37] at five locations (covering all composition regions) determined on the sections removed from the middle of the FGM blocks as shown in Fig. 4. For each of the specimens, the stresses were planned to be measured along the building direction (BD) based on the relative position of the austenite phase diffraction peak (042) nominally appearing at 2 θ = 146.65° by the radiation wavelength of Cu-K_α (λ = 1.540598 Å). The residual stress calculations were carried out using STRESS software provided by Malvern PANalytical, in which the following equations were used to convert the lattice strain at an incident angle of ψ to the surface normal and a measurement angle of ϕ ($\varepsilon_{\phi\psi}$) to the stress at the ϕ angle (σ_ϕ):

$$\varepsilon_{\phi\psi} = \left(\frac{1+\nu}{E}\right)\sigma_\phi\ sin^2\ \psi - \left(\frac{\nu}{E}\right)(\sigma_{xx}+\sigma_{yy}) \tag{3}$$

$$\varepsilon_{\phi\psi} = \frac{d_{\phi\psi} - d_0}{d_0} \tag{4}$$

where ν is the Poisson's ratio, E is the elastic modulus, σ_{xx} and σ_{yy} are the principal stresses and $d_{\phi\psi}$ and d_0 are respectively the atomic plane spacing at the ϕ and ψ angles and the stress-free spacing. Then, σ_ϕ can be obtained by substituting Eq. (4) into (3) and differentiating it with respect to $sin^2\ \psi$, as below:

$$\sigma_\phi = \left(\frac{1+\nu}{E}\right).\frac{1}{d_0}\left(\frac{\partial d_{\phi\psi}}{\partial sin^2\ \psi}\right) \tag{5}$$

Additionally, to improve the accuracy of the measurement results for individual materials, an attempt was made for the F25 specimen to

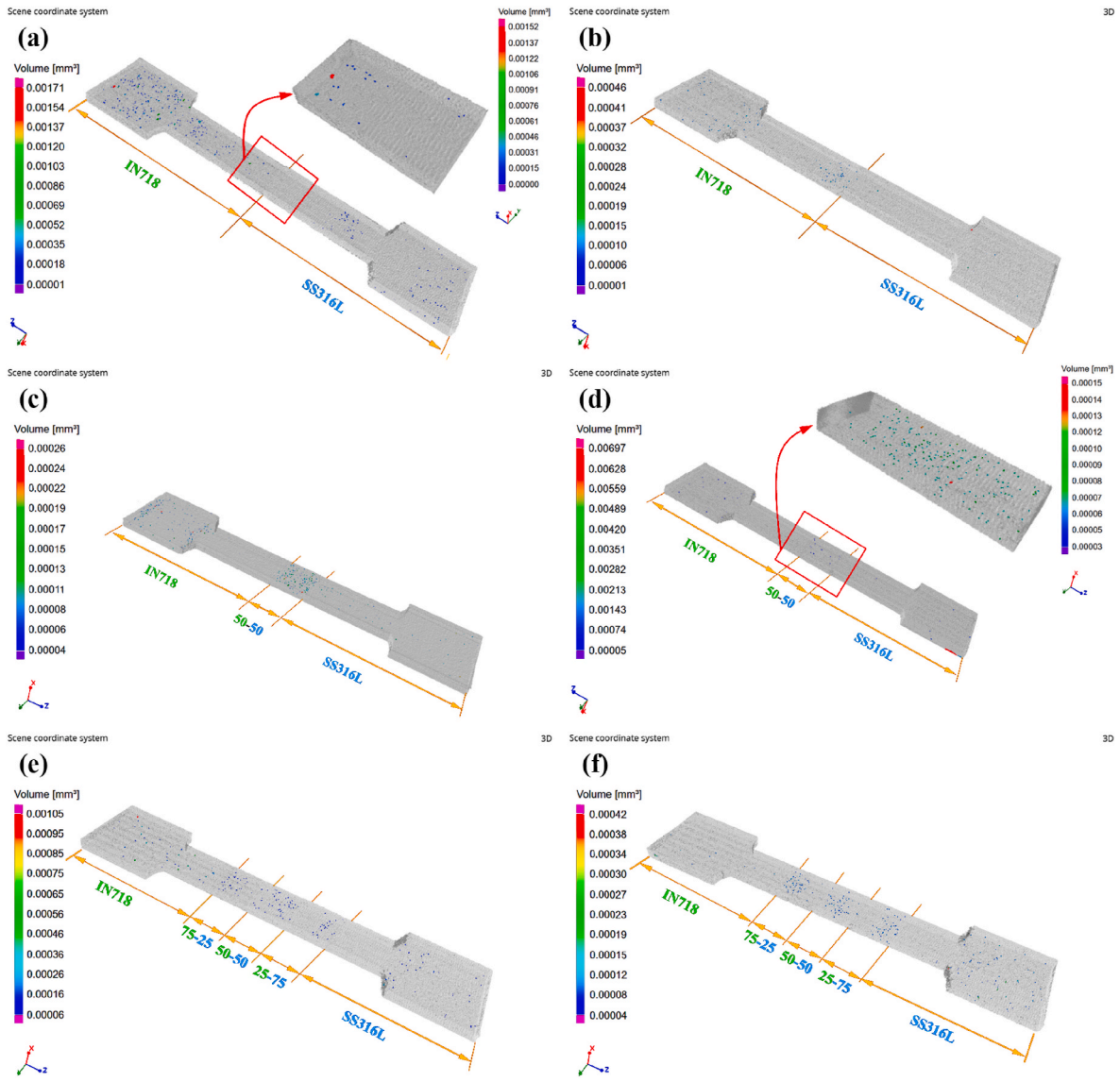

Fig. 5. 3D CT scan images of the tensile samples: a) F0.L, b) F0.Opt, c) F50SS.Opt, d) F50IN.Opt, e) F25.L, and F25.Opt.

realize the measurement by radiation of a chromium cathode, which generates characteristic radiation with a wavelength of $\lambda = 2.289760$ Å. For that radiation, the diffraction peak (220) is located around $2\theta = 130^{\circ}$ similar for all compositional regions owing to the close affinity of the base alloys (See Table 4). It was supposed that using a longer wavelength would make it possible to separate the diffraction reflections coming from the crystal structures of SS316L and IN718, thus making it possible to calculate the stresses separately for each material.

Lastly, the uniaxial tensile test (Instron 5500R, UK) at a crosshead rate of 2 mm/min was conducted on the FGM samples fabricated for this purpose, and the results including yield strength (0.2 % offset), tensile strength (ultimate stress at necking), elongation (strain to fracture), and toughness (integral of the area under the stress-strain curve), were reported as mean values ± standard deviations (STDs). Subsequently, the fracture surfaces were evaluated by SEM to complement the understanding of the mechanical behavior of FGMs.

3. Results and discussion

Fig. 5 displays 3D CT images of the FGM tensile samples, on which the extent of the composition regions was determined. Overall, the volume of internal defects in all samples is evaluated as slight according to the legend of the images, which means the FGMs fabricated by L-PBF have an acceptable density (>99 %). Nevertheless, a comparison between the F0.L and F0.Opt samples in Fig. 5a and b, respectively, indicate that the samples produced with the optimum (Opt) *VED* contain much smaller numbers and volumes of internal defects, as expected. This is also confirmed for F25.L (Fig. 5e) and F25.Opt (Fig. 5f) samples. However, a concentration of internal defects can be found in the gradient regions (Fig. 5c–f) regardless of L/Opt *VED*, because the process parameters were considered based on pure alloy regions, and the interaction of laser and materials in the gradient regions is different. That is why significantly fewer defects have been formed in the 50 wt% mixed region of the F50IN.Opt sample (Fig. 5d) compared to F50SS.Opt (Fig. 5c) since, in the former, the intermediate region was made by *VED* similar to that of the IN718 region, which is higher than the *VED* of the SS316L region (119 > 90 J/mm^3). However, several defects were still detected in the localized CT of F50IN.Opt (the selected area in Fig. 5d) with a lower voxel size, which can be accounted infinitesimal given their size scale. Hence, that composition region in F25 samples was intentionally built by the same *VED* as the IN718 region.

The macrostructure evaluation of the various composition regions in the F25 sample (Fig. 6) as a representative of other samples reveals notable characteristics. First, the melt pool geometry seems to change

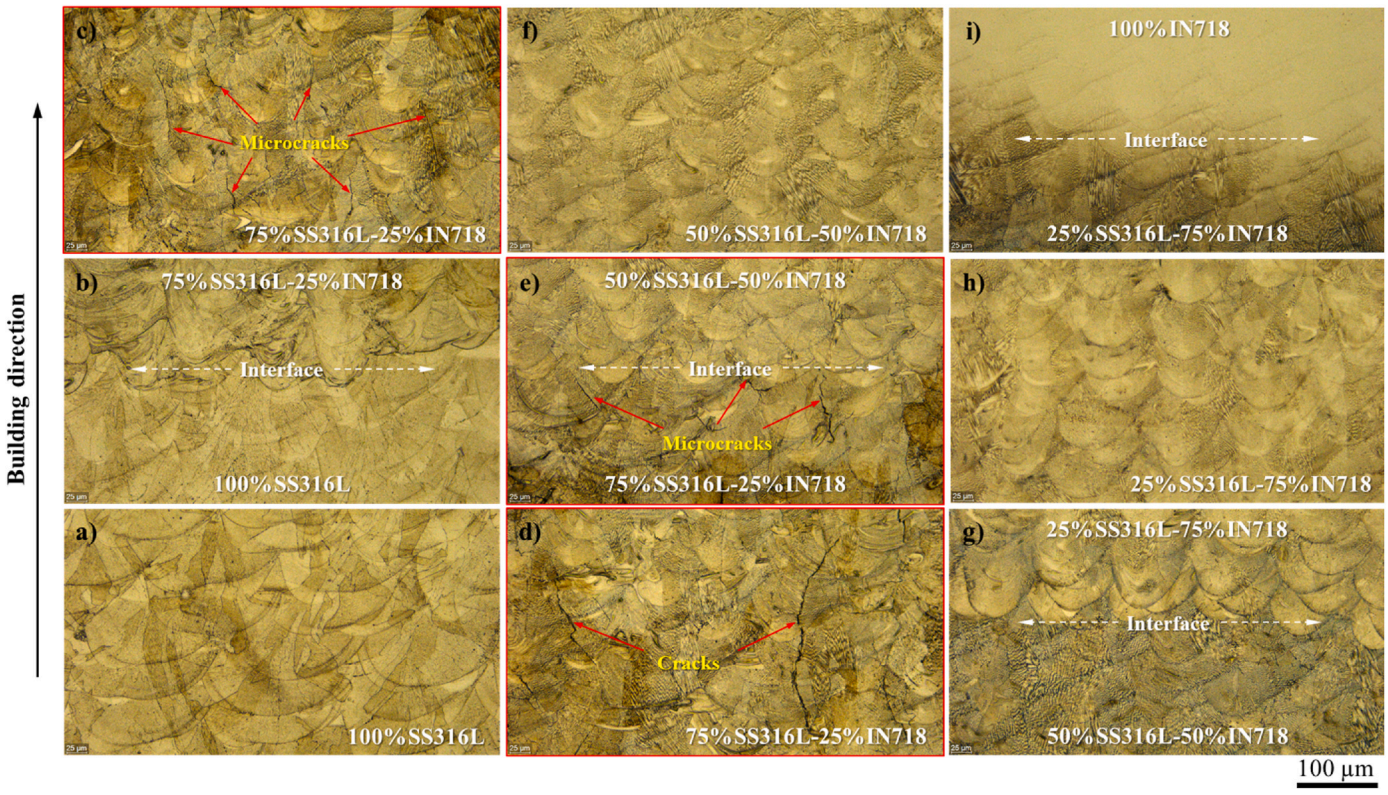

Fig. 6. Macrostructure of various composition regions and their interface in the F25.Opt sample along the building direction: a) SS316L, b) SS316L | 75-25 interface, c, d) 75-25, e) 75-25| 50-50 interface, f) 50–50, g) 50-50| 25-75 interface, h) 25–75, and i) 25-75| IN718 interface.

along the building direction from the SS316L region in Fig. 6a to the subsequent regions and the topmost region in Fig. 6i. This is attributed to i) the reduced heat dissipation via conduction downward to the substrate and ii) using higher *VED* for the upper composition regions (specifically, from the 50-50 region to the top), which led to an increase in the depth of the melt pool along the building direction [38,39]. Second, good metallurgical bonding has been formed at the interfaces (Fig. 6b–e, g, and i), and almost no evident internal porosity can be found through the sample, which is also in line with the CT results. However, severe cracking is observed in the 75-25 composition region (Fig. 6c, d, and e), where, in some cases, the length of a crack reaches more than 200 µm (Fig. 6d). The serrated edge of the cracks indicates hot cracking that is discussed in the following to elucidate their underlying formation mechanisms.

Microstructural evolution across the composition regions of the F25.Opt sample is illustrated at different magnifications in Fig. 7. As can be seen, the microstructure morphology has gradually evolved from cellular (Fig. 7e–d) to cellular-dendritic (Fig. 7c) and eventually to dendritic (Fig. 7b–a) along the building direction, caused by the disruption of the solidification front stability based on the constitutional supercooling criterion [40,41]:

$$\frac{G_L}{R} \geq \frac{m_L C_\infty (k-1)}{k D_L} \tag{6}$$

where G_L is the gradient temperature in the liquid at the solidification interface, R is the advancing velocity of the solidification front, m_L is the liquidus line slope, C_∞ is the bulk solute concentration, k is the equilibrium partition coefficient, and D_L is the liquid diffusivity. As the FGM height rises, the temperature gradient (G_L) reduces due to heat accumulation and using higher *VED* (50-50 region to the top). Additionally, the higher contribution of IN718 rich in alloying elements, including molybdenum and niobium, leads to an increase in C_∞ and a decrease in the k on the right side of the above inequality. These factors result in a growing instability of the solidification front, according to Eq. (6), and the transition of the solidification structure from cellular to dendritic along the building direction. This phenomenon was also demonstrated via numerical modeling elsewhere [39]. In addition to the variation of solidification morphology, its size has also coarsened along the building direction (compare Fig. 7a1-e1 or a2-e2) due to the reduced temperature gradient, and consequently lower cooling rate ($\dot{\varepsilon}$) in the upper regions [39,40]:

$$\lambda_d = b\dot{\varepsilon}^{-n} \tag{7}$$

where λ_d is the cellular/dendrite arm spacing (C/DAS), and b and n are the material constants. Furthermore, considerable contrasts of micro-segregations and secondary phases at sub-grain boundaries relative to the matrix can be observed in every composition region, which is more easily visible at the highest magnification (Fig. 7a2-e2). They seem to be aggravated along the building direction as the contribution of IN718 increases, and the reduced cooling rate provides more time for the diffusion and partitioning of alloying elements [42]. Delta ferrite in the SS316L region and Laves in the gradient and IN718 regions are the possible secondary phases along with the gamma (γ) matrix phase, which were also identified in a similar study [43] and further analyzed by EDS in the following. Moreover, some oxide inclusions can be found in the SS316L and 75-25 composition regions indicated by purple arrows in Fig. 7e2 and d2, which might originate from the recycled powder feedstock (*esp.*, SS316L) or the oxidation during the process as also demonstrated and addressed in detail elsewhere [44]. The reason that why it couldn't be found in other sections may attributed to reduced their fraction and size with increasing contribution of higher purity IN718 powder (than SS316L powder as the main source of the impurities) and using higher volumetric energy density (VED) along the building direction, as a lower concentration of oxide inclusions in the 75-25 section can be observed compared to the SS316L section. The continuous elemental segregation (Fig. 7d), as well as the presence of

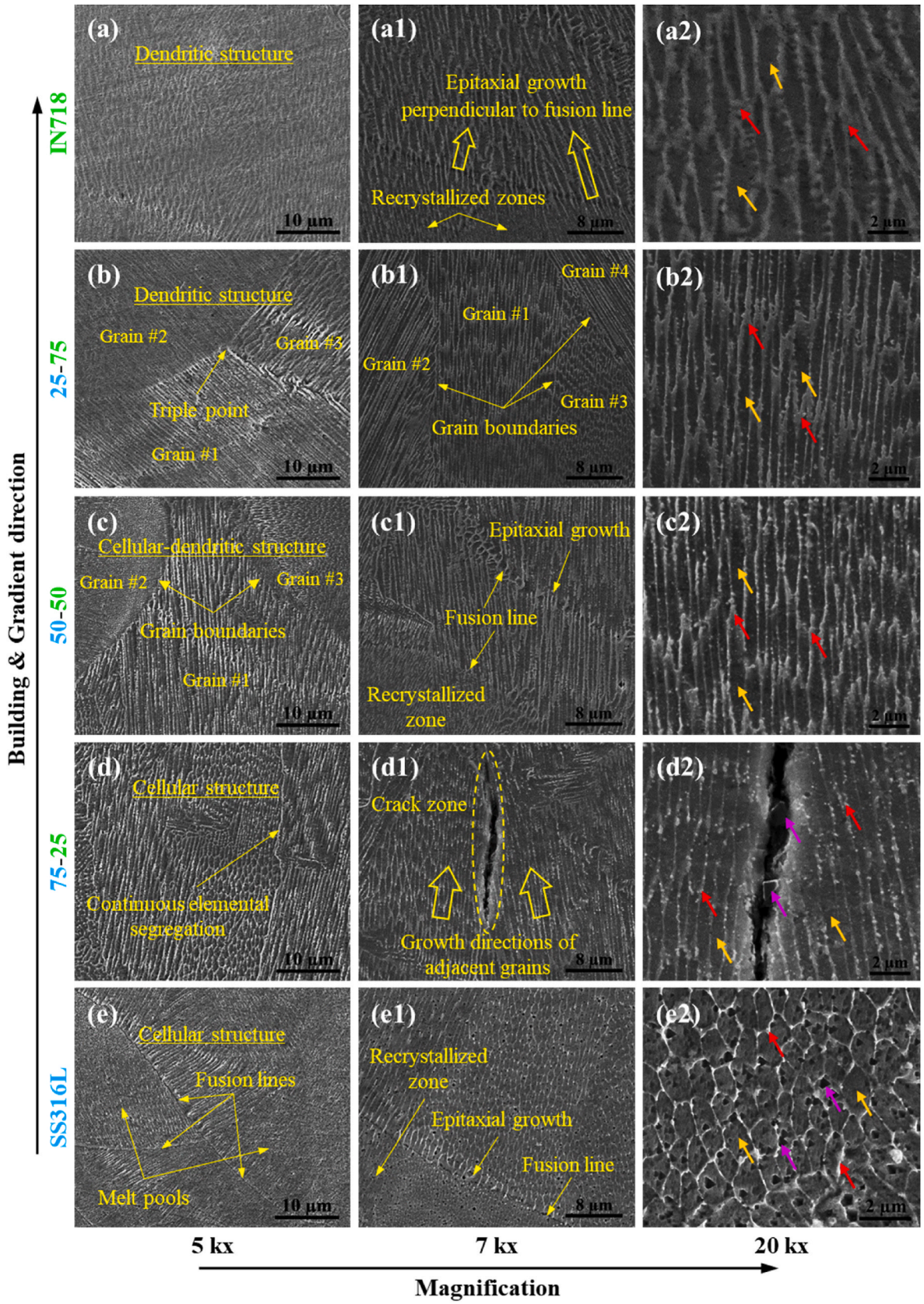

Fig. 7. Microstructure of various composition regions in the F25.Opt samples along the building direction at different magnifications: a) IN718 [35], b) 25–75, c) 50–50, d) 75-25 [35], and e) SS316L. The orange, red, and purple arrows in (a2-e2) indicate the matrix, secondary phase, and oxide inclusion, respectively. (For interpretation of the references to colour in this figure legend, the reader is referred to the Web version of this article.)

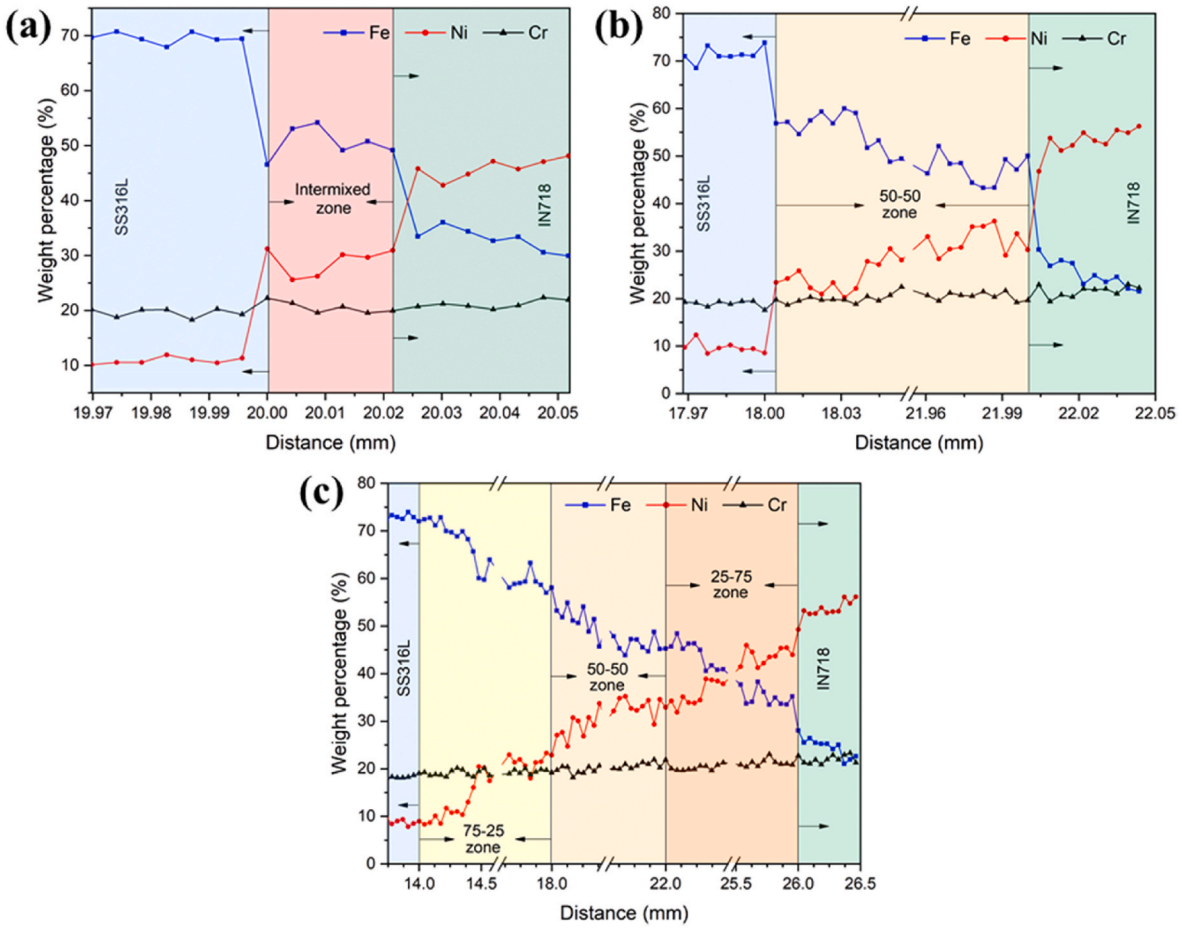

Fig. 8. Distribution of main alloying elements (Fe, Ni, Cr) in the FGMs along the building direction: a) F0, b) F50 (present study), and c) F25 [35].

oxide inclusions (Fig. 7d2) in the 75-25 composition region, can induce crack formation at the solidification grain boundary (Fig. 7d1), as also reported by Kim et al. [20] in the DED process. In fact, the elemental segregation increases the brittle temperature range (BTR), and the oxide inclusion exacerbates the microstructure decohesion, both of which provide conditions for the nucleation of solidification cracks, which later propagate along the grain boundary influenced by thermal stresses raised from printing subsequent layers.

Fig. 8 shows the distribution of the main alloying elements (Fe, Ni, and Cr) at the interface zones of the FGM samples along the building direction. Despite the discrete design of the F0 sample, an intermixed zone has been formed between the pure SS316L and IN718 regions (Fig. 8a) due to the dilution effect, though it could not prevent the drastic compositional change at the interface as the remelted layer is basically superficial in the L-PBF process. In contrast, the drastic change in composition has been effectively modified by the F50 design and almost eliminated in the F25 sample, as shown in Fig. 8b and c, respectively, which could potentially improve the part performance by reducing the difference in properties of adjacent regions.

In Fig. 9, the elemental distribution maps of a cracked area in the 75-25 composition region of the F25 sample indicate micro-segregations of C, O, Si, Mo, and Nb elements inside and at the edge of the crack. Although EDS is a semi-quantitative analysis and not very accurate for light elements, the relatively high concentration of C inside the crack can be attributed to the metal carbide formed in that region, as also declared by Carroll et al. [45]. Besides, the concentrated O and Si elements in the same location inside the crack could indicate the presence of oxide inclusions such as silicon oxides (SiO_2), encouraging crack nucleation. Also, the inhomogeneous distributions of Mo and Nb elements, more clearly distinguished in Fig. 10 by EDS point analysis from the matrix (Fig. 10c) and the crack origin (Fig. 10d), indicate that they segregated along sub-grain and grain boundaries due to very low partition coefficients ($k \ll 1$) during the solidification process. It has led to Laves phase formation through the low-temperature eutectic reaction of $L \rightarrow \gamma +$ Laves [43], as it was demonstrated using thermodynamic calculations that a high fraction of Laves phase would form in around 25 wt% IN718 [23]. Therefore, it essentially increases the BTR and susceptibility to solidification cracking in the 75-25 composition region of the F25 sample.

The results of EBSD analysis integrated with EDS at the SS316L | IN718 interface of the F0 sample are shown in Fig. 11. The intermixed (diluted) zone between the terminal alloys can be recognized on the Fe and Ni distribution maps in Fig. 11a and b with about 130 μm width. The inverse pole figure (IPF) map and pole figures (PFs) in Fig. 11c–f, respectively, indicate a preferred grain orientation in {100} plane (parallel to BD) and inclined to <110> due to the localized maximum temperature gradient downward to the substrate. The orientation seems to become straighter and rather stronger in the IN718 region (upper half of the IPF map) owing to the higher *VED* and enhanced epitaxial growth. Hence, coarser grains and relatively lower density of grain boundary can be observed in this region in the grain size distribution map (Fig. 11d) and high/low angle grain boundary (H/LAGB) visualization map (Fig. 11e), respectively.

Fig. 12 shows EBSD results at the SS316L | 50-50 and 50-50| IN718 interfaces of the F50(IN) sample along each other in the building direction. The IPF maps (Fig. 12a–e) and PFs (Fig. 12d and e) reveal that the grain structure orientation has evolved from {100}<110> at the SS316L | 50-50 interface to a strong texture of {100}<100> at the 50-

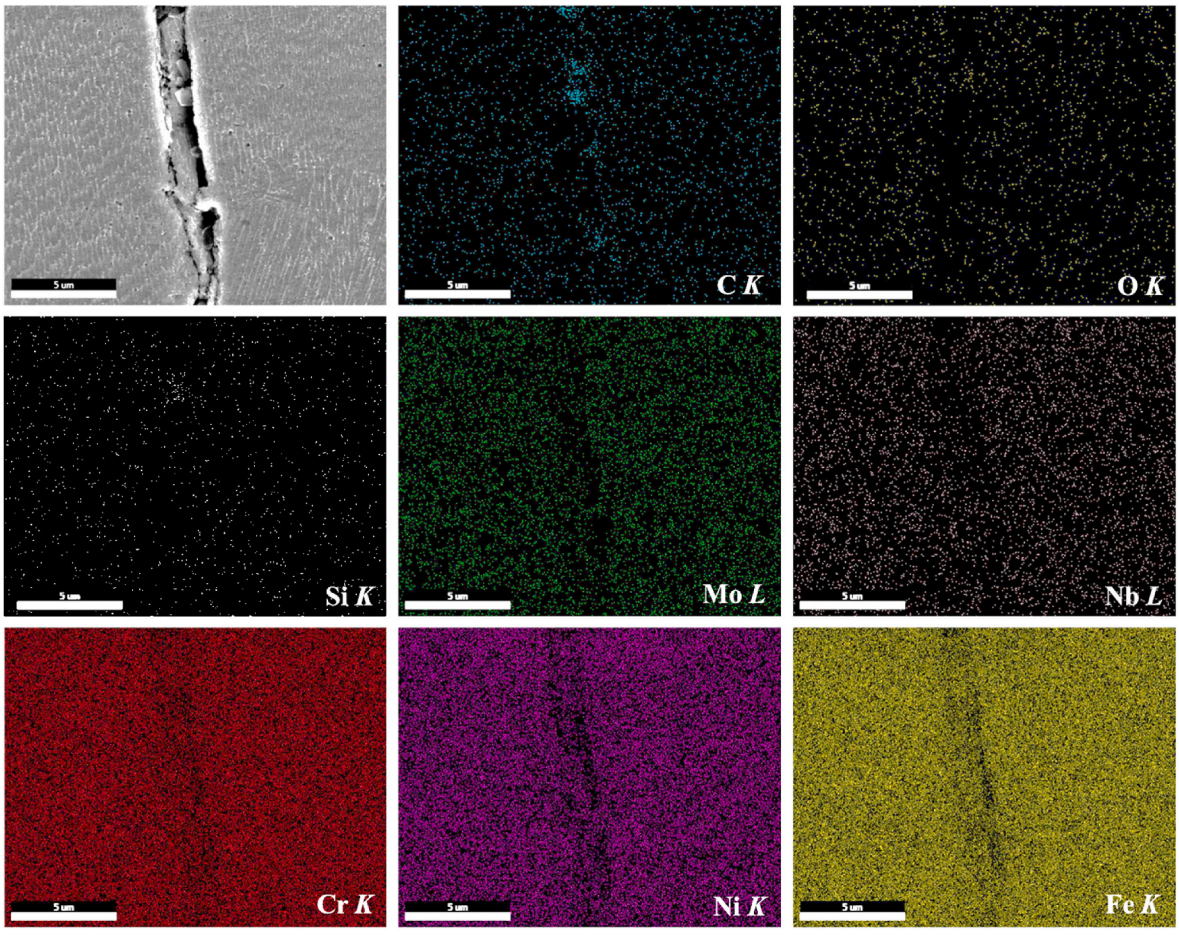

Fig. 9. SEM micrograph and the corresponding elemental distribution maps from a crack area in the 75-25 composition region of the F25 sample.

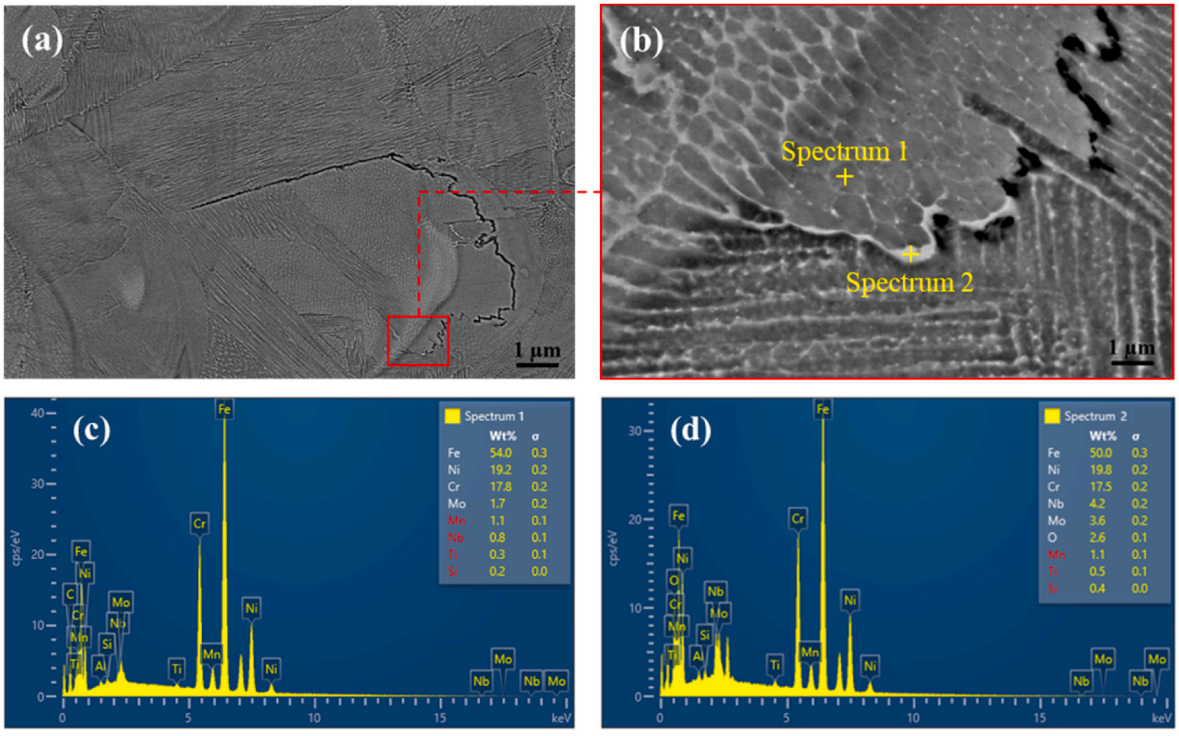

Fig. 10. a) Crack morphology in the 75-25 composition region, b) higher magnification of the selected area in (a), and c, d) EDS analysis from the targeted microstructural features 1 and 2 in (b), respectively.

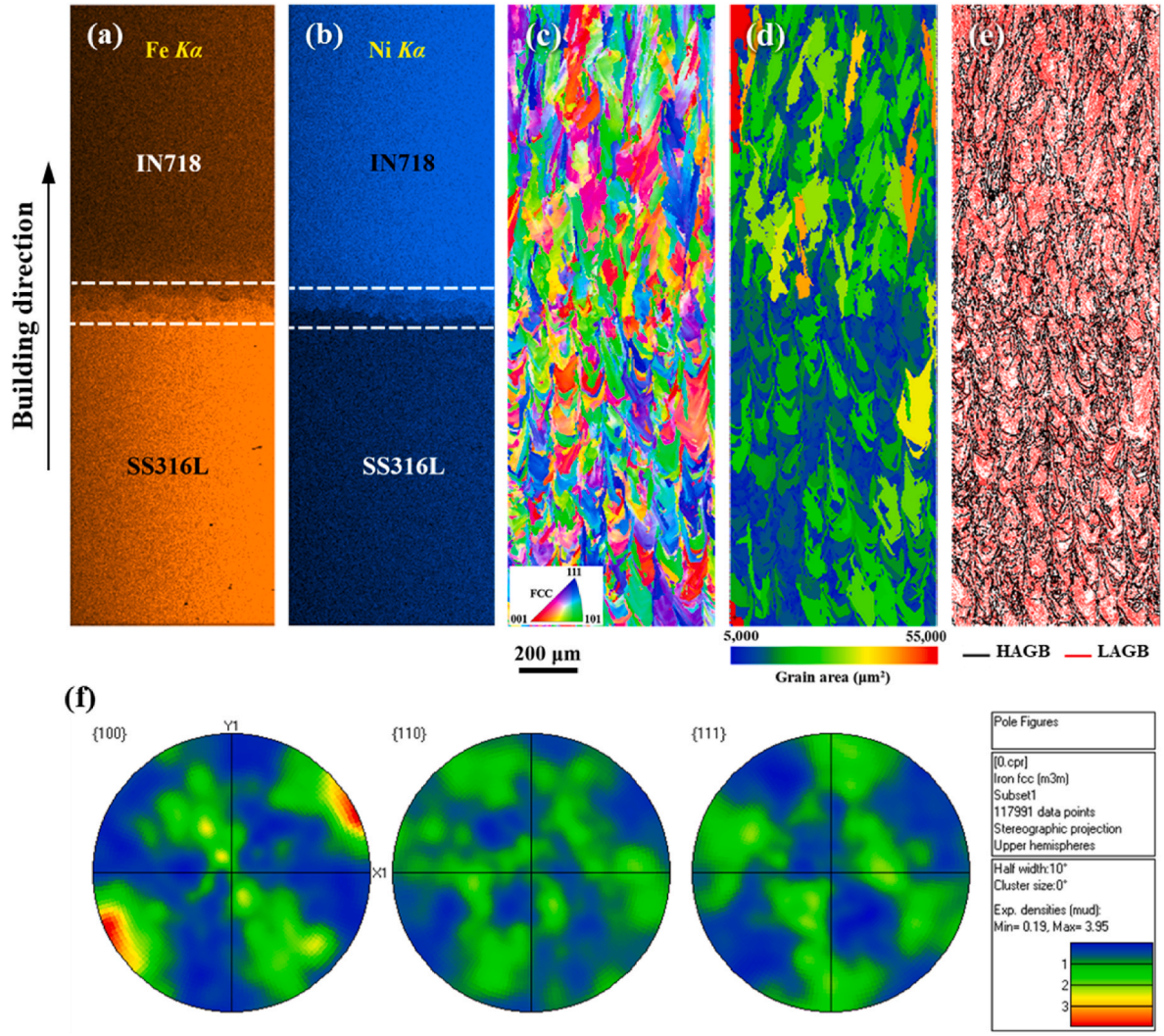

Fig. 11. a, b) Ni and Fe distribution, c) IPF X, d) grain size distribution, e) H/LAGB maps [35], and f) PFs of {100}, {110}, and {111} planes at the SS316L | IN718 interface of the F0 sample. The dashed lines in (a, b) surround the intermixed zone.

50| IN718 interface since higher *VED* was used for both 50-50 and IN718 regions, which deepens the melt pool and enhances epitaxial columnar growth. Likewise, a considerably lower density of grain boundary (Fig. 12b–f) and crystal defect in the kernel average misorientation (KAM) distribution maps (Fig. 12c–g) were obtained from the 50-50 composition region to the top compared to SS316L region.

Moving forward to the F25 sample, the IPF maps and PFs from its interfaces in Fig. 13 indicate a sinusoidal grain structure evolution along the building direction, meaning that it begins with a randomized texture (Fig. 13d, d1), then to a preferred ({100}<110>, Fig. 13c, c1), then back again to a randomized (Fig. 13b, b1), and finally evolves to a dominant texture ({100}<100>/<110>) at the top (Fig. 13a, a1). This can be attributed that first the heat accumulation disrupts the preferred orientation at SS316L | 75-25 interface, then using higher *VED* for the 50-50 region restores the temperature gradient for textural grain evolution at the 75-25 | 50-50 interface, while the high configurational entropy of the 25–75 composition [46] disrupts the texture again at the 50-50 | 25-75 interface, though it finally reforms at the top passing through the 25–75 region.

That textural evolution in the range of 75-25 composition region could be another reason behind the continuous elemental microsegregation encouraging intergranular crack propagation, as also declared elsewhere [47]. In this regard, the EBSD analysis from a crack area of this composition region in Fig. 14 clearly demonstrates that the crack was formed in the intergranular spacing and propagated along the (high angle) grain boundaries. Also, the crystal defects in the KAM map (Fig. 14d) indicate localized plastic deformations at the crack tip, the moderate intensity of which suggests an easy crack propagation along the grain boundaries as high energy areas.

Fig. 15 shows residual stresses measured at the predetermined locations on the FGM structures' surface (Fig. 4) along the building direction. The measurements indicate tensile residual stresses for each of the samples along the measurement length, and more importantly, the dynamics of the stress gradient changes by the FGM design (Fig. 15a). In the F0 sample, there is a sharp change in stress from around 100 MPa to around 300 MPa. However, these variations become more gradual in the F50 sample. Meanwhile, they are smooth and almost imperceptible in the F25 sample owing to closer material properties tailored in the interface regions. These modified stress variations by the FGM design were similarly demonstrated in the DED process using finite element (FE) modeling by Ghanavati et al. [48]. Moreover, although the theoretical assumptions on the XRD measurement differences utilizing Cu-K_α and Cr-K_α wavelengths are correct, they cannot be realized for the F25 sample in Fig. 15b. Nevertheless, it confirms the correctness of the results obtained by the copper cathode irradiation experiment: the stress values along the F25 sample remained at a same level throughout the entire length of the test section.

The tensile test results of all FGM structures produced by the L and

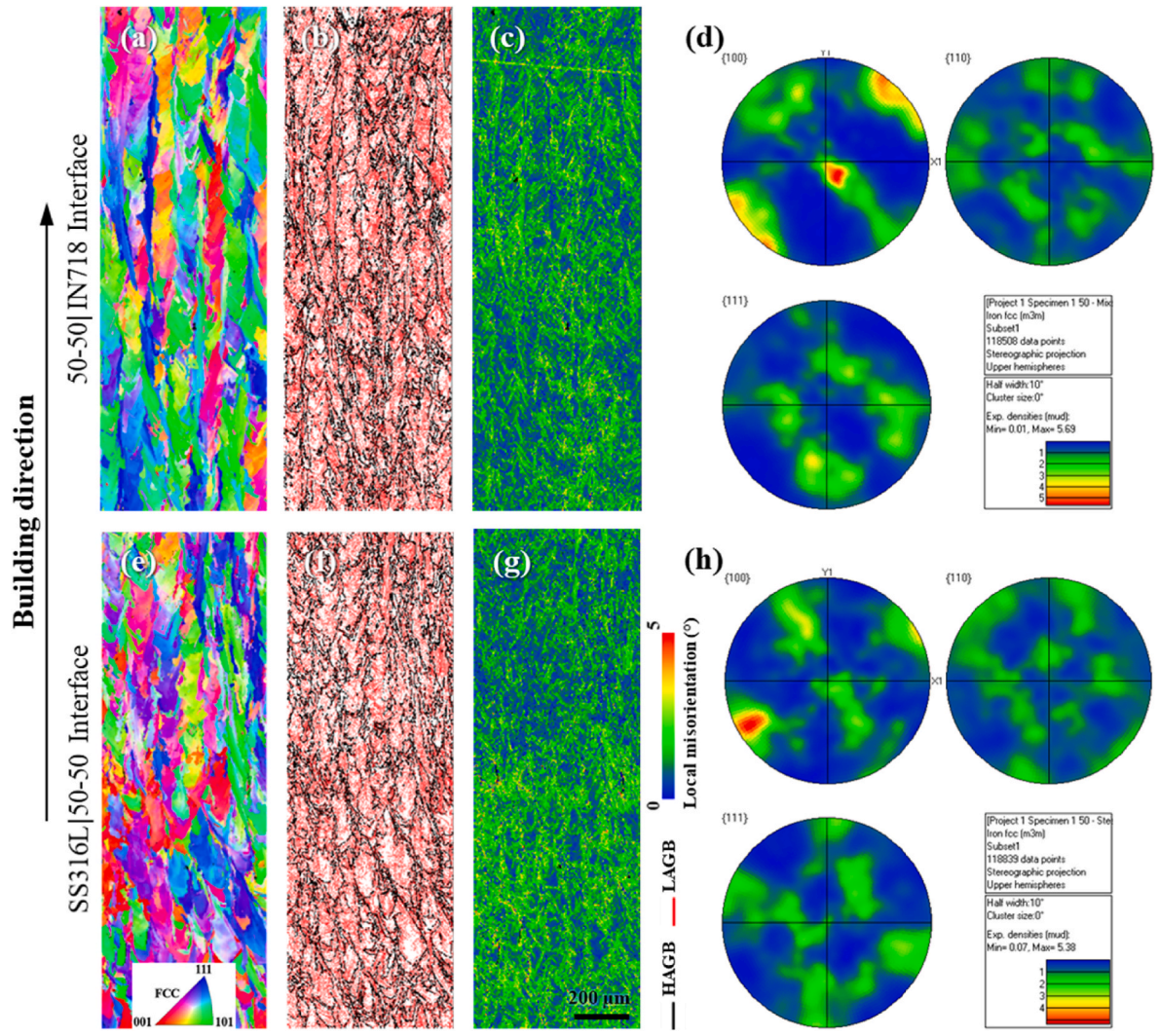

Fig. 12. a-d) IPF X, H/LAGB, KAM distribution maps, and PFs, respectively, at the 50-50 | IN718 interface and e-h) IPF X, H/LAGB, KAM distribution maps, and PFs, respectively, at the SS316L | 50-50 interface of the F50(IN) sample.

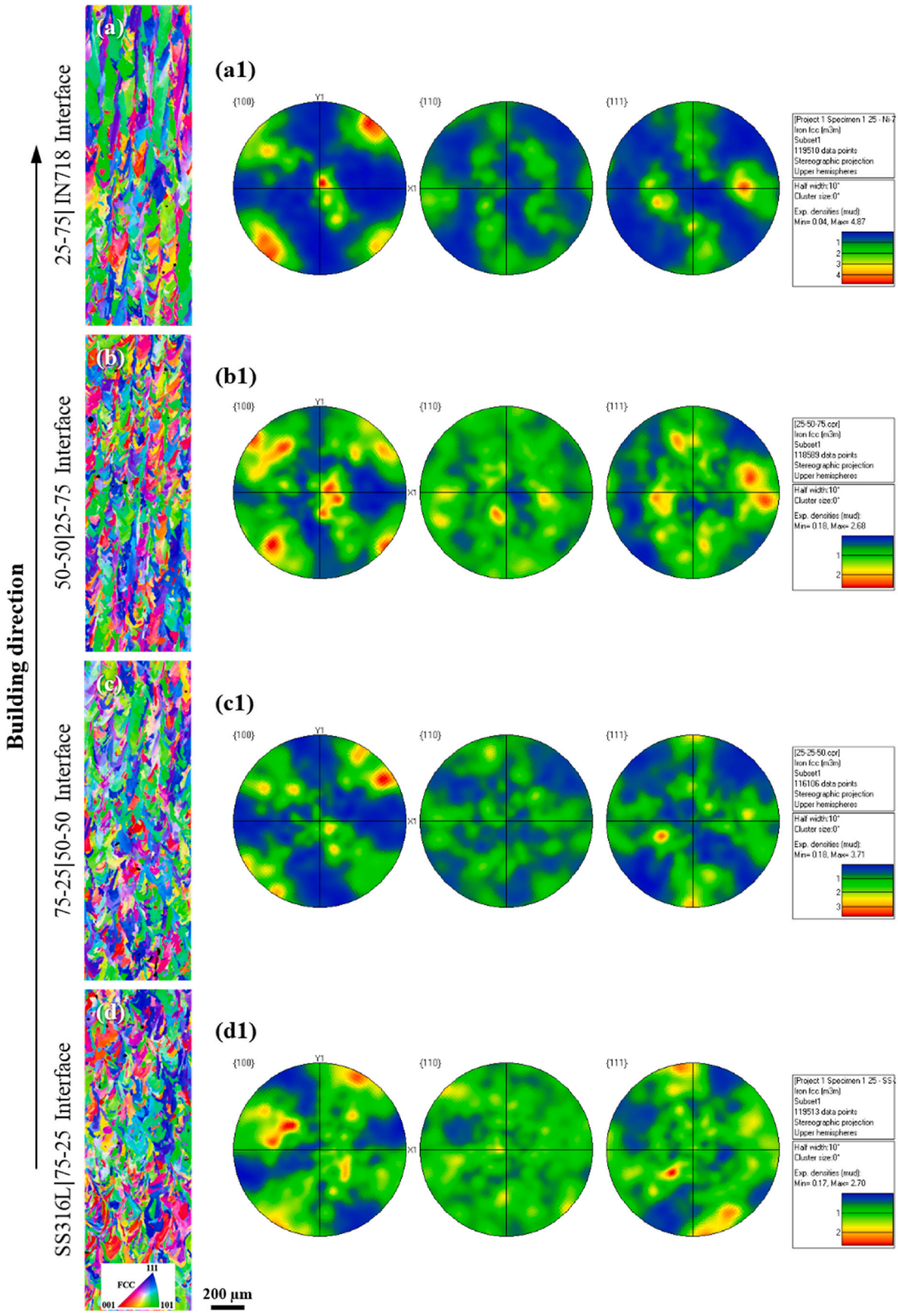

Fig. 13. IPF X maps and the corresponding PFs at the interfaces of the F25 sample: a) 25-75 | IN718, b) 50-50 | 25-75, c) 75-25| 50–50, d) SS316L | 75-25.

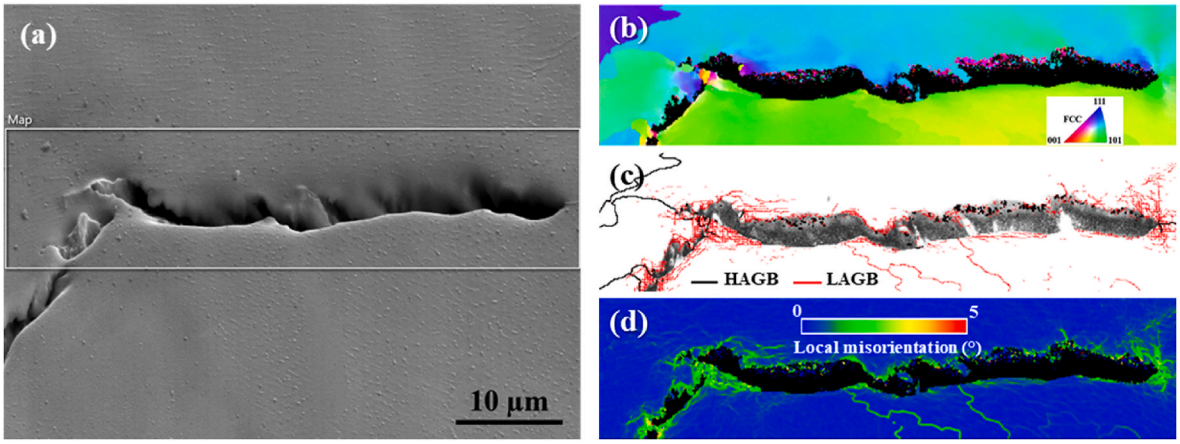

Fig. 14. a) SEM image of a crack in the susceptible 75-25 composition region and b, c, d) the EBSD analysis with IPF X, H/LAGB, and KAM maps, respectively, from the selected area in (a).

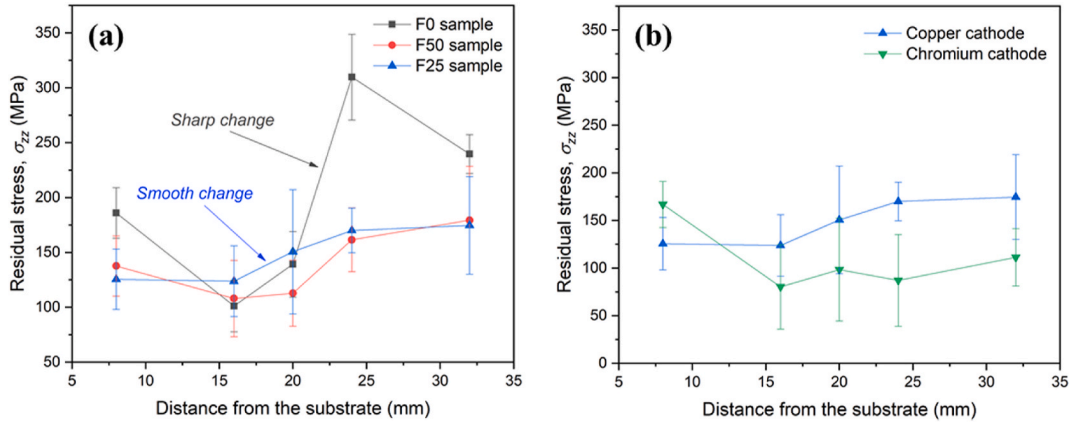

Fig. 15. Residual stress (Z-component, σ_{zz}) variations along the building direction in a) different FGM structures and b) F25 samples utilizing different X-ray wavelengths of copper and chromium cathodes in the XRD measurement technique.

Opt *VED* levels as well as fractured tensile samples, are presented in Fig. 16. The comparison of stress-strain curves of FGM.Opt samples (Fig. 16a) indicate that the F50IN.Opt has the highest strength and ductility, as it can provide an effectively modified residual stress distribution and more uniform deformation with a 50 wt% mixed intermediate region compared to F0.Opt, and also minimum internal defects compared to the F50SS.Opt and F25.Opt. In contrast, F25.As expected, the opt sample exhibits the poorest tensile properties due to the solidification cracking in its 75-25 composition region. That is why the fracture in the F25 sample occurred with almost a flat surface in the range of that defective composition region, while other samples fractured at the SS316L region (as the weakest terminal alloy) with the typical cup-and-cone appearances, as shown in Fig. 16b also indicating strong metallurgical bonding at the interfaces. Further, an individual comparison of each FGM.Opt with its L type (Fig. 16c–f) reveals that FGM.L samples (except F25.L) are generally stronger but fail earlier, which can be respectively attributed to finer grain structures caused by the higher cooling rate but more internal porosities. However, the F25.L sample exclusively shows both higher strength and ductility than F25.Opt due to the lower cracking susceptibility during the fabrication process using the lower *VED*. A holistic assessment of the tensile properties in Fig. 17 specifies that the F50IN.Opt owns the best performance, recording mean values of 510 MPa yield strength, 610 MPa tensile strength, 31.5 % elongation, and 17.6 kJ/mm^3 toughness, against the worst performance, which belongs to the F25.Opt with mean values of 510 MPa yield strength, 580 MPa tensile strength, 11 % elongation, and 6 kJ/mm^3 toughness. Nevertheless, the mechanical properties of FGMs fabricated by the L-PBF process in this study are higher than those reported in similar studies by the DED process such as Ref. [21], which can be associated with the inherent difference between the two processes, including higher sensitivity to surface/internal defects and coarser microstructures in the DED process.

Macro-scale fractrography of the FGM.Opt tensile samples in Fig. 18 distinguish the F25 fracture surface (Fig. 18d) from others with remarkable propagated solidification cracks, resulting in limited plastic deformation and premature failure. Besides, some voids can be observed in the F50SS fracture surface, which may be raised by the process disorder. Further details by the SEM micrographs from the center and edge of the fracture surfaces illustrated in Fig. 19 reveal a fully ductile fracture for F0, F50SS, and F50IN tensile samples in the presence of microvoids and equiaxed/spherical dimples at the center and elongated dimples indicating shear lips at the edge of their fracture surfaces (Fig. 19a1-a3, b1-b3, and c1-c3, respectively). However, the F25 fracture surface determines a combination of dominant brittle and ductile fracture mechanisms by identifying the cleavage planes and river pattern due to the rapid propagation of the pre-existed solidification cracks at its center (Fig. 19d1, d2) and elongated dimples at its edge (Fig. 19d3).

4. Conclusions

In this research, an innovative approach was adopted to design and

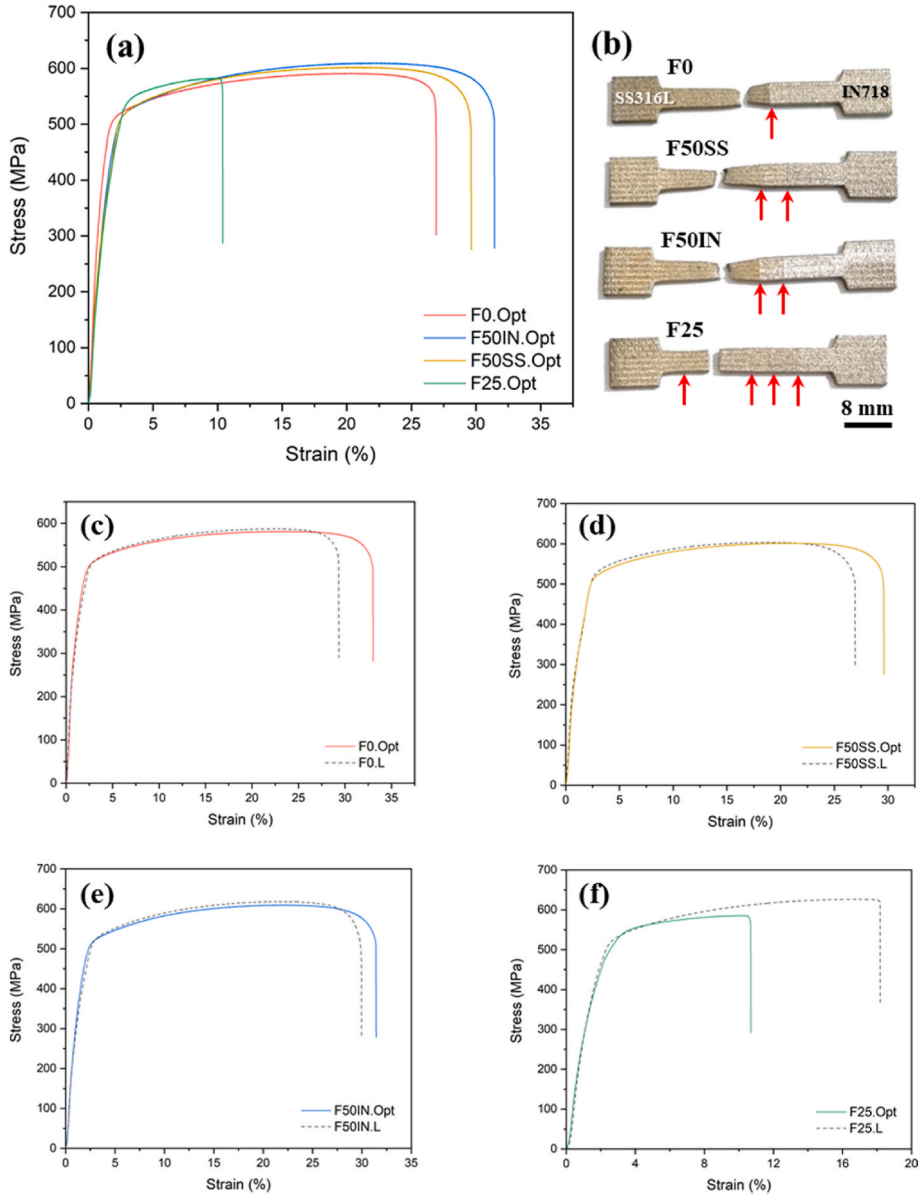

Fig. 16. Tensile test results: a) Engineering stress-strain diagram of FGM samples produced by Opt *VED* [35], b) fractured tensile samples (the arrows show interfaces of the composition regions), and c-f) individual comparison of stress-strain curves of F0, F50SS, F50IN, and F25 samples, respectively, produced by the L and Opt *VED* s.

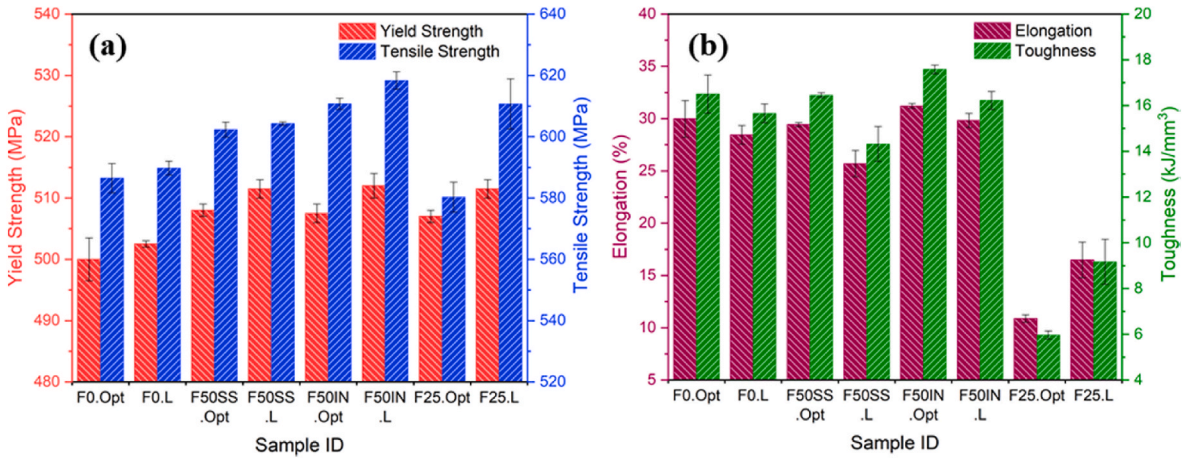

Fig. 17. Comparison of a) yield and tensile strengths as well as b) elongation and toughness of FGM structures produced by the different *VED* levels.

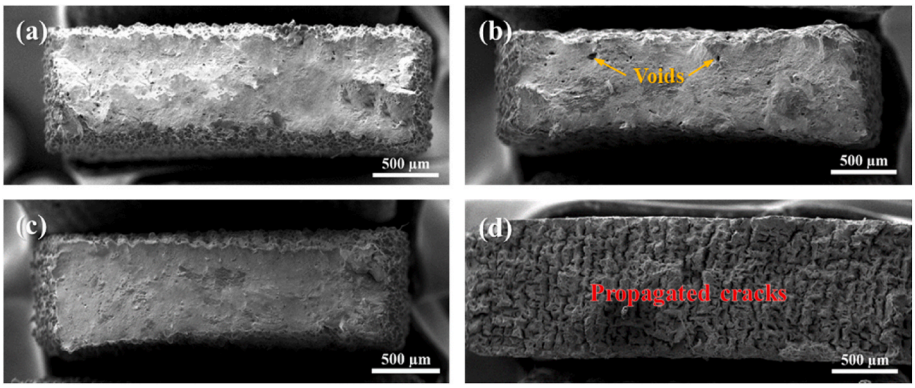

Fig. 18. Fracture surfaces of the FGM.Opt tensile samples in macro-scale: a) F0, F50SS, c) F50IN, and d) F25.

develop SS316L-IN718 functionally graded materials (FGMs) using a standard laser powder bed fusion (L-PBF) process. High-throughput characterization tests were systematically performed to realize the effects of FGM design (F0, F50, and F25) and processing conditions on the microstructure and mechanical properties of the samples with different weight fractions of the two phases at the interface region. In the following, the most important findings of this study are summarized:

1) The evaluation of internal defects by X-ray computed tomography (CT) revealed that all FGM samples have an acceptable density throughout their height, demonstrating the reliability and reproducibility of the process and proper development of the process window, although a few concentrated small volume defects were detected in the gradient regions owing to different interaction of laser and material in those regions. Moreover, the FGMs density was further enhanced using optimum volumetric energy densities (*VED* s) for the pure regions and based on that for gradient regions.
2) In the FGM structure with 25 wt% gradient steps (F25), the 75-25 composition region was found highly susceptible to solidification crack nucleating around oxide inclusions at the inter-cellular/dendritic elemental microsegregation, which increases brittle temperature range (BTR) with the low-temperature eutectic reaction of L $\rightarrow \gamma +$ Laves. Further, a textural evolution of the grain structure demonstrated in the range of that region aggravates the continuity of the microsegregation and encourages intergranular crack propagation influenced by thermal stresses during the process.
3) The dynamics of the residual stress variations along the building direction are effectively modified by the FGM design from a sharp change ($\Delta\sigma_{zz} = 200$ MPa) in the bimetal (F0) structure to a gradual variation in the FGM with a 50 wt% mixed intermediate region (F50) to a smooth change in the F25 structure caused by closing material properties of adjacent regions, which could potentially improve the sample's performance.
4) The assessment of tensile properties indicated that the FGM with a 50 wt% mixed intermediate region fabricated by the optimum *VED* (F50IN.Opt) has the best performance with a fully ductile fracture at the SS316L region and the mean values of 510 MPa yield strength, 610 MPa tensile strength, 31.5 % elongation, and 17.6 kJ/mm^3 toughness. In contrast, the F25.Opt, suffering from severe solidification cracking in the 75-25 composition region, recorded the weakest tensile properties with a combination of dominant brittle and ductile fracture mechanisms caused by rapid crack propagation in the susceptible region and limited plastic deformation.

CRediT authorship contribution statement

Reza Ghanavati: Writing – original draft, Visualization, Software, Methodology, Investigation, Formal analysis, Data curation. **Abdollah Saboori:** Writing – review & editing, Validation, Supervision, Resources, Project administration, Funding acquisition, Conceptualization. **Elżbieta Gadalińska:** Writing – review & editing, Visualization, Formal analysis, Data curation. **Sara Bagherifard:** Writing – review & editing, Resources. **Luca Iuliano:** Writing – review & editing, Resources, Funding acquisition.

Declaration of competing interest

The authors declare that they have no known competing financial

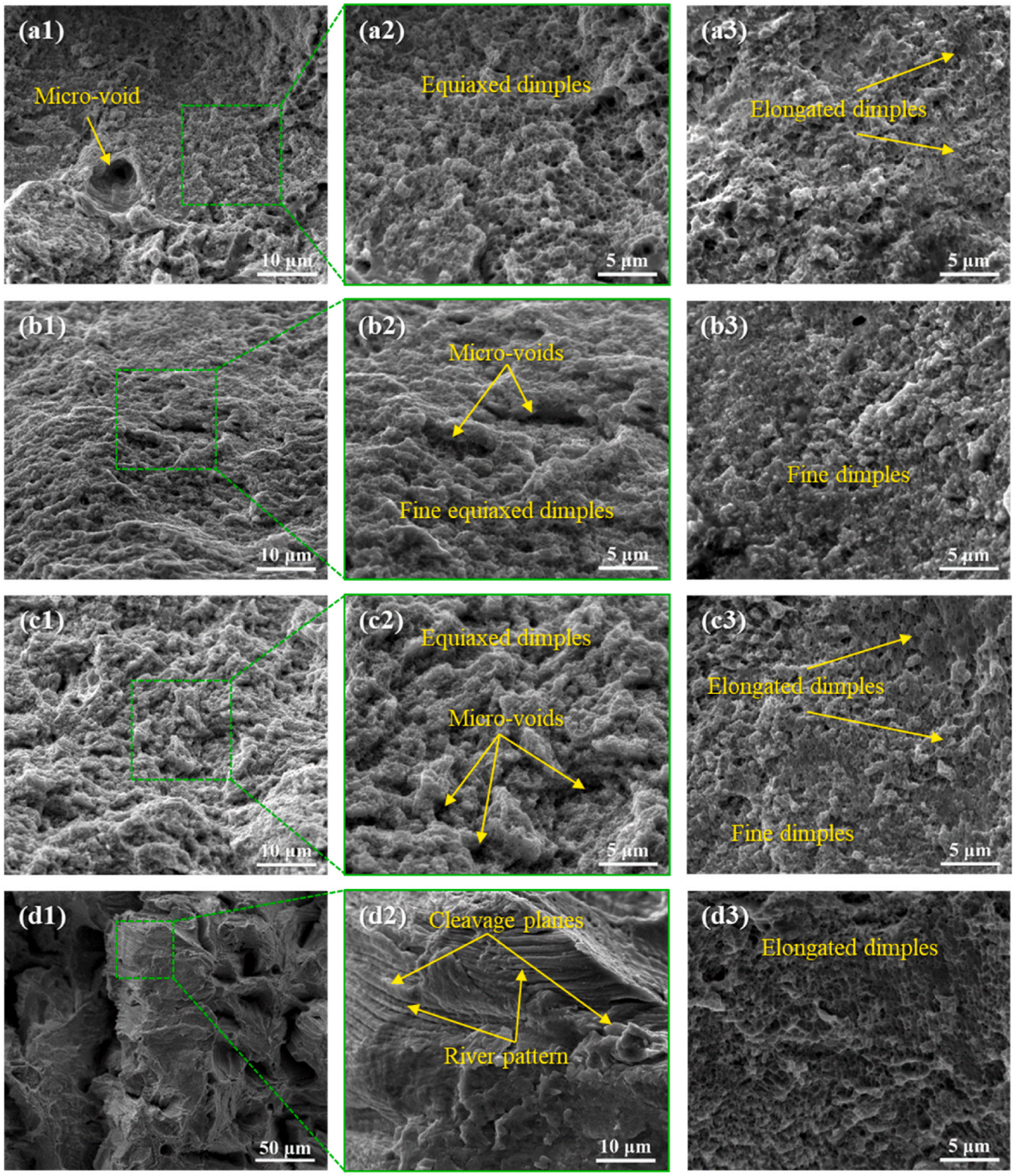

Fig. 19. SEM micrographs from the a1-d1) center and a3-d3) edge of fracture surfaces of the FGM.Opt tensile samples shown in Fig. 18: a1-a3) F0, b1-b3) F50SS, c1-c3) F50IN, d1-d3) F25. The selected areas in (a1-d1) are provided at a higher magnification in (a2-d2).

interests or personal relationships that could have appeared to influence the work reported in this paper.

Data availability

Data will be made available on request.

References

[1] M. Naebe, K. Shirvanimoghaddam, Functionally graded materials: a review of fabrication and properties, Appl. Mater. Today 5 (2016) 223–245.
[2] R. Ghanavati, H. Naffakh-Moosavy, Additive manufacturing of functionally graded metallic materials: a review of experimental and numerical studies, J. Mater. Res. Technol. 13 (2021) 1628–1664.
[3] I.M. El-Galy, B.I. Saleh, M.H. Ahmed, Functionally graded materials classifications and development trends from industrial point of view, SN Appl. Sci. 1 (2019) 1–23.
[4] B. Saleh, J. Jiang, R. Fathi, T. Al-hababi, Q. Xu, L. Wang, D. Song, A. Ma, 30 years of functionally graded materials: an overview of manufacturing methods, applications and future challenges, Compos. B Eng. 201 (2020) 108376.
[5] C. Zhang, F. Chen, Z. Huang, M. Jia, G. Chen, Y. Ye, Y. Lin, W. Liu, B. Chen, Q. Shen, L. Zhang, Additive manufacturing of functionally graded materials: a review, Mater. Sci. Eng. A 764 (2019) 138209.
[6] A. Reichardt, A.A. Shapiro, R. Otis, R.P. Dillon, J.P. Borgonia, B.W. McEnerney, P. Hosemann, A.M. Beese, Advances in additive manufacturing of metal-based functionally graded materials, Int. Mater. Rev. 66 (1) (2021) 1–29.
[7] M.H. Mosallanejad, R. Ghanavati, A. Behjat, M. Taghian, A. Saboori, L. Iuliano, Untapped opportunities in additive manufacturing with metals: from new and graded materials to post-processing, Metals 14 (4) (2024) 425.
[8] D.R. Feenstra, R. Banerjee, H.L. Fraser, A. Huang, A. Molotnikov, N. Birbilis, Critical review of the state of the art in multi-material fabrication via directed energy deposition, Curr. Opin. Solid State Mater. Sci. 25 (4) (2021) 100924.

[9] D. Wang, L. Liu, G. Deng, C. Deng, Y. Bai, Y. Yang, W. Wu, J. Chen, Y. Liu, Y. Wang, X. Lin, Recent progress on additive manufacturing of multi-material structures with laser powder bed fusion, Virtual Phys. Prototyp. 17 (2) (2022) 329–365.
[10] F. Hengsbach, P. Koppa, M.J. Holzweissig, M.E. Aydinöz, A. Taube, K.P. Hoyer, O. Starykov, B. Tonn, T. Niendorf, T. Tröster, M. Schaper, Inline additively manufactured functionally graded multi-materials: microstructural and mechanical characterization of 316L parts with H13 layers, Prog. Addit. Manuf. 3 (2018) 221–231.
[11] M.G. Scaramuccia, A.G. Demir, L. Caprio, O. Tassa, B. Previtali, Development of processing strategies for multigraded selective laser melting of Ti6Al4V and IN718, Powder Technol. 367 (2020) 376–389.
[12] C. Wei, L. Liu, Y. Gu, Y. Huang, Q. Chen, Z. Li, L. Li, Multi-material additive-manufacturing of tungsten-copper alloy bimetallic structure with a stainless-steel interlayer and associated bonding mechanisms, Addit. Manuf. 50 (2022) 102574.
[13] J. Knörlein, M.M. Franke, M. Schloffer, T. Berger, C. Körner, Microstructure and mechanical properties of additively manufactured γ-TiAl with dual microstructure, Intermetallics 161 (2023) 107978.
[14] P. Daram, T. Hiroto, M. Watanabe, Microstructure and phase evolution of functionally graded multi-materials of Ni–Ti alloy fabricated by laser powder bed fusion process, J. Mater. Res. Technol. 23 (2023) 5559–5572.
[15] H. Guo, D. Liu, M. Xu, Z. Dong, L. Zhang, Preparation, characterization and composition optimization design of laser powder bed fusion continuously graded Invar36/316L stainless steel alloys, Mater. Char. 209 (2024) 113709.
[16] L. Deillon, N.A. Beldarrain, X. Li, M. Bambach, Coupling hot isostatic pressing and laser powder bed fusion: a new strategy to manufacture defect-free CuCrZr-316L steel multi-material structures, Mater. Des. 241 (2024) 112914.
[17] K. Shah, I. ul Haq, A. Khan, S.A. Shah, M. Khan, A.J. Pinkerton, Parametric study of development of Inconel-steel functionally graded materials by laser direct metal deposition, Mater. Des. 54 (2014) 531–538.
[18] C. Sun, Y. Wang, M.D. McMurtrey, N.D. Jerred, F. Liou, J. Li, Additive manufacturing for energy: a review, Appl. Energy 282 (2021) 116041.
[19] D. Melzer, J. Džugan, M. Koukolíková, S. Rzepa, J. Vavřík, Structural integrity and mechanical properties of the functionally graded material based on 316L/IN718 processed by DED technology, Mater. Sci. Eng. A 811 (2021) 141038.
[20] S.H. Kim, H. Lee, S.M. Yeon, Jr C. Aranas, K. Choi, J. Yoon, S.W. Yang, H. Lee, Selective compositional range exclusion via directed energy deposition to produce a defect-free inconel 718/SS 316L functionally graded material, Addit. Manuf. 47 (2021) 102288.
[21] S.W. Yang, J. Yoon, H. Lee, D.S. Shim, Defect of functionally graded material of inconel 718 and STS 316L fabricated by directed energy deposition and its effect on mechanical properties, J. Mater. Res. Technol. 17 (2022) 478–497.
[22] W. Li, M.N. Kishore, R. Zhang, N. Bian, H. Lu, Y. Li, D. Qian, X. Zhang, Comprehensive studies of SS316L/IN718 functionally gradient material fabricated with directed energy deposition: multi-Physics & multi-materials modelling and experimental validation, Addit. Manuf. 61 (2023) 103358.
[23] K. Li, J. Zhan, M. Zhang, R. Ma, Q. Tang, D.Z. Zhang, L.E. Murr, H. Cao, A functionally graded material design from stainless steel to Ni-based superalloy by laser metal deposition coupled with thermodynamic prediction, Mater. Des. 217 (2022) 110612.
[24] J. Lu, W. Li, Improvement of tensile properties of laser directed energy deposited IN718/316L functionally graded material via different heat treatments, Mater. Sci. Eng. A 866 (2023) 144694.
[25] G. Xu, R. Wu, K. Luo, J. Lu, Effects of heat treatment on hot corrosion behavior of directed energy deposited In718/316L functionally graded material, Corros. Sci. 197 (2022) 110068.
[26] Y. Li, M. Koukolíková, J. Džugan, M. Brázda, High temperature fracture behavior of 316L stainless steel-inconel 718 functionally graded materials manufactured by directed energy deposition: role of interface orientation and heat treatment, Mater. Sci. Eng. A 898 (2024) 146389.
[27] A. Hinojos, J. Mireles, A. Reichardt, P. Frigola, P. Hosemann, L.E. Murr, R. B. Wicker, Joining of inconel 718 and 316 stainless steel using electron beam melting additive manufacturing technology, Mater. Des. 94 (2016) 17–27.
[28] X. Mei, X. Wang, Y. Peng, H. Gu, G. Zhong, S. Yang, Interfacial characterization and mechanical properties of 316L stainless steel/inconel 718 manufactured by selective laser melting, Mater. Sci. Eng. A 758 (2019) 185–191.
[29] W.Y. Chen, X. Zhang, M. Li, R. Xu, C. Zhao, T. Sun, Laser powder bed fusion of inconel 718 on 316 stainless steel, Addit. Manuf. 36 (2020) 101500.
[30] S.M. Yusuf, X. Zhao, S. Yang, N. Gao, Interfacial characterisation of multi-material 316L stainless steel/Inconel 718 fabricated by laser powder bed fusion, Mater. Lett. 284 (2021) 128928.
[31] M.S. Duval-Chaneac, N. Gao, R.H. Khan, M. Giles, K. Georgilas, X. Zhao, P.A. Reed, Fatigue crack growth in IN718/316L multi-materials layered structures fabricated by laser powder bed fusion, Int. J. Fatig. 152 (2021) 106454.
[32] W.W. Wits, E. Amsterdam, Graded structures by multi-material mixing in laser powder bed fusion, CIRP Ann. 70 (1) (2021) 159–162.
[33] V. Errico, P. Posa, A. Fusco, A. Angelastro, S.L. Campanelli, Intralayer multi-material structure stainless-steel/nickel-superalloy fabricated via laser-powder bed fusion process, Manuf. Lett. 35 (2023) 11–15.
[34] Y. Wen, J. Gao, R.L. Narayan, P. Wang, L. Zhang, B. Zhang, U. Ramamurty, X. Qu, Microstructure-property correlations in as-built and heat-treated compositionally graded stainless steel 316L-Inconel 718 alloy fabricated by laser powder bed fusion, Mater. Sci. Eng. A 862 (2023) 144515.
[35] R. Ghanavati, E. Lannunziata, E. Norouzi, S. Bagherifard, L. Iuliano, A. Saboori, Design and development of SS316L-IN718 functionally graded materials via laser powder bed fusion, Mater. Lett. 349 (2023) 134793.
[36] P.J. Withers, H.K. Bhadeshia, Residual stress. Part 1–measurement techniques, Mater. Sci. Technol. 17 (4) (2001) 355–365.
[37] A. Lodh, K. Thool, I. Samajdar, X-ray diffraction for the determination of residual stress of crystalline material: an overview, Trans. Indian Inst. Met. 75 (4) (2022) 983–995.
[38] T. DebRoy, H.L. Wei, J.S. Zuback, T. Mukherjee, J.W. Elmer, J.O. Milewski, A. M. Beese, A.D. Wilson-Heid, A. De, W. Zhang, Additive manufacturing of metallic components–process, structure and properties, Prog. Mater. Sci. 92 (2018) 112–224.
[39] R. Ghanavati, H. Naffakh-Moosavy, M. Moradi, M. Eshraghi, Printability and microstructure of directed energy deposited SS316l-IN718 multi-material: numerical modeling and experimental analysis, Sci. Rep. 12 (1) (2022) 16600.
[40] R. Mehrabian, Rapid solidification, Int. Met. Rev. 27 (1) (1982) 185–208.
[41] J.P. Oliveira, A.D. LaLonde, J. Ma, Processing parameters in laser powder bed fusion metal additive manufacturing, Mater. Des. 193 (2020) 108762.
[42] C. Kumara, A.R. Balachandramurthi, S. Goel, F. Hanning, J. Moverare, Toward a better understanding of phase transformations in additive manufacturing of alloy 718, Materialia 13 (2020) 100862.
[43] R. Ghanavati, H. Naffakh-Moosavy, M. Moradi, Additive manufacturing of thin-walled SS316L-IN718 functionally graded materials by direct laser metal deposition, J. Mater. Res. Technol. 15 (2021) 2673–2685.
[44] A. Saboori, A. Aversa, F. Bosio, E. Bassini, E. Librera, M. De Chirico, S. Biamino, D. Ugues, P. Fino, M. Lombardi, An investigation on the effect of powder recycling on the microstructure and mechanical properties of AISI 316L produced by directed energy deposition, Mater. Sci. Eng. A 766 (2019) 138360.
[45] B.E. Carroll, R.A. Otis, J.P. Borgonia, J.O. Suh, R.P. Dillon, A.A. Shapiro, D. C. Hofmann, Z.K. Liu, A.M. Beese, Functionally graded material of 304L stainless steel and inconel 625 fabricated by directed energy deposition: characterization and thermodynamic modeling, Acta Mater. 108 (2016) 46–54.
[46] N. Sargent, Y. Wang, D. Li, Y. Zhao, X. Wang, W. Xiong, Exploring alloy design pathway through directed energy deposition of powder mixtures: a study of stainless steel 316L and Inconel 718, Additive Manuf. Lett. 6 (2023) 100133.
[47] R. Ghanavati, H. Naffakh-Moosavy, M. Moradi, F. Mazzucato, A. Valente, S. Bagherifard, A. Saboori, Design optimization for defect-free AISI 316 L/IN718 functionally graded materials produced by laser additive manufacturing, Mater. Char. 220 (2025) 114697.
[48] R. Ghanavati, H. Naffakh-Moosavy, M. Moradi, E. Gadalińska, A. Saboori, Residual stresses and distortion in additively-manufactured SS316L-IN718 multi-material by laser-directed energy deposition: a validated numerical-statistical approach, J. Manuf. Process. 108 (2023) 292–309.